



HAL
open science

Effect of the local clay distribution on the effective electrical conductivity of clay rocks

P. Cosenza, D. Pret, M. C. Zamora

► **To cite this version:**

P. Cosenza, D. Pret, M. C. Zamora. Effect of the local clay distribution on the effective electrical conductivity of clay rocks. *Journal of Geophysical Research: Solid Earth*, 2015, 120, pp.145-168. 10.1002/2014JB011429 . hal-01331798

HAL Id: hal-01331798

<https://hal.science/hal-01331798>

Submitted on 12 Nov 2021

HAL is a multi-disciplinary open access archive for the deposit and dissemination of scientific research documents, whether they are published or not. The documents may come from teaching and research institutions in France or abroad, or from public or private research centers.

L'archive ouverte pluridisciplinaire **HAL**, est destinée au dépôt et à la diffusion de documents scientifiques de niveau recherche, publiés ou non, émanant des établissements d'enseignement et de recherche français ou étrangers, des laboratoires publics ou privés.

Copyright

RESEARCH ARTICLE

10.1002/2014JB011429

Key Points:

- Relationships between electrical conductivity and clay distribution in rocks
- Relationships between electrical conductivity and clay rock microstructure
- A local clay theory to infer effective electrical conductivity of clay rocks

Correspondence to:

P. Cosenza,
philippe.cosenza@univ-poitiers.fr

Citation:

Cosenza, P., D. Prêt, and M. Zamora (2015), Effect of the local clay distribution on the effective electrical conductivity of clay rocks, *J. Geophys. Res. Solid Earth*, 120, 145–168, doi:10.1002/2014JB011429.

Received 10 JUL 2014

Accepted 26 NOV 2014

Accepted article online 4 DEC 2014

Published online 26 JAN 2015

Effect of the local clay distribution on the effective electrical conductivity of clay rocks

P. Cosenza¹, D. Prêt¹, and M. Zamora²

¹IC2MP-HydrASA Poitiers, Université de Poitiers, CNRS, UMR 7285, Poitiers, France, ²Institut de Physique du Globe de Paris, Sorbonne Paris Cité, Université Paris Diderot, UMR 7154 CNRS, Paris, France

Abstract The “local porosity theory” proposed by Hilfer was revisited to develop a “local clay theory” (LCT) that establishes a quantitative relationship between the effective electrical conductivity and clay distribution in clay rocks. This theory is primarily based on a “local simplicity” assumption; under this assumption, the complexity of spatial clay distribution can be captured by two local functions, namely, the local clay distribution and the local percolation probability, which are calculated from a partitioning of a mineral map. The local clay distribution provides information about spatial clay fluctuations, and the local percolation probability describes the spatial fluctuations in the clay connectivity. This LCT was applied to (a) a mineral map made from a Callovo-Oxfordian mudstone sample and (b) (macroscopic) electrical conductivity measurements performed on the same sample. The direct and inverse modeling shows two results. First, the textural and classical model assuming that the electrical anisotropy of clay rock is mainly controlled by the anisotropy of the sole clay matrix provides inconsistent inverted values. Another textural effect, the anisotropy induced by elongated and oriented nonclayey grains, should be considered. Second, the effective conductivity values depend primarily on the choice of the inclusion-based models used in the LCT. The impact of local fluctuations of clay content and connectivity on the calculated effective conductivity is lower.

1. Introduction

Clay rocks are currently under investigation as potential host rocks for high-level radioactive waste repositories in several industrial countries. This interest can be explained by the following two properties [e.g., *Pusch*, 2006]: (1) because of their high-specific surface area, clay rocks can absorb a significant amount of ions and (2) they have low-hydraulic conductivities (typically of the order of $10^{-13} \text{ m s}^{-1}$). These particular physicochemical properties are mainly controlled by the type and the amount of clay minerals that are present in argillaceous rock. But clay rocks are rarely pure clayey materials. They often contain accessory minerals (up to 40 wt %), such as quartz and carbonates, which can affect their mechanical properties [e.g., *Vasin et al.*, 2013] as well as their transport properties [e.g., *Horseman et al.*, 1996].

The effect of the microscopic organization of the accessory minerals (or its counterpart the microscopic clay organization) on the transport properties of clay rocks has been investigated both experimentally and theoretically. Considering experimental studies, their objective was to establish qualitative relationships between microscopic patterns obtained from imaging techniques (e.g., Scanning Electron Microscopy (SEM), electronic microprobe analysis, X-ray microtomography, analysis of diffraction images, and autoradiography) and the tortuosity of diffusion paths. On the basis of SEM element distribution maps and porosity maps obtained by autoradiographic method, *Sammartino et al.* [2003] identified that carbonate content determines Callovo-Oxfordian (COx) mudstone microstructure by its large aggregates and elongated bioclasts, thus influencing on the accessible pore volume and the tortuosity. *Robinet et al.* [2007, 2012] and *David et al.* [2007] confirmed the existence of a preferential orientation of carbonates and quartz, leading to partial control of the macroscopic diffusion anisotropy measured in the COx mudstone. *Wenk et al.* [2007, 2008] characterized also the preferential orientation of minerals of two clay rocks (COx mudstone from France and Opalinus clay from Switzerland) by using X-ray diffraction. Their results show that both investigated clay rocks exhibit a significant alignment of clay minerals and calcite. The authors also extracted from their data quantitative information about phase fractions and their preferential orientation (i.e., orientation distribution), which could be used to model macroscopic physical properties. More recently, *Keller et al.* [2011] used Focused Ion Beam tomography to construct 3-D microstructures of pore space of three samples taken from Mont-Terri site (i.e., Opalinus clay) with a resolution of 10 nm. The resulting voxel-based

representation of the 3-D pore structure was numerically converted into a skeleton. This skeleton representation allowed for calculations of orientation data (i.e., pore path orientation) and associated numerical values (i.e., pore path length and pore path tortuosity). These analyses confirmed again that the microstructure of Opalinus clay rock shows a preferential orientation parallel to the bedding plane in combination with a lower pore path tortuosity in this plane. Pore path tortuosity perpendicular to the bedding plane was observed to be higher by a factor of as much as 5, but a large part of the pore space (pores smaller than 10 nm) was not accounted for in this analysis whereas these pores correspond to pore throats deeply impacting the tortuosity of the medium.

At this stage, although these petrographic observations provided insights in identifying the relevant microstructural patterns involved in the transport mechanisms in clay rocks, their quantitative connection to macroscopic measurements of transport properties, especially electrical conductivity, is still a critical issue. Indeed, these petrographic observations are not integrated in conventional theoretical approaches used for modeling macroscopic electrical conductivity.

To our knowledge, there exist three distinct approaches to calculate effective electrical conductivity: (1) semi-empirical approaches mainly based on Archie's relationship, (2) numerical models, and (3) effective medium approximations (EMAs).

In the first group, the empirical concepts of "formation factor" F and "characteristic pore size" Λ [e.g., Sen, 1997; Sen *et al.*, 1997; Jougnot *et al.*, 2009, 2010; Leroy and Revil, 2009; Zisser and Nover, 2009; Revil and Florsch, 2010; Revil *et al.*, 2013] are preferentially used. These approaches do not require a fine description of the clay rock microstructure, since the latter is embedded in the parameters F and Λ . In the second group, numerical methods are used for solving the Laplace equation for various random packings of spheres and ellipsoidal particles [e.g., Coelho *et al.*, 1997; Paszkuta *et al.*, 2006] or for microstructural units (i.e., clay platelets and/or aggregates) [e.g., Tabbagh *et al.*, 2002; Tabbagh and Cosenza, 2007]. Nevertheless, these works based on sophisticated calculations performed for idealized clayey geomaterials did not account for the actual spatial organization of clay minerals and their associated accessory minerals.

In the third group, i.e., in the effective medium theories, the effective electrical conductivity is calculated by using inclusion-based models that view the clay rock as a clay matrix with randomly embedded spherical or ellipsoidal inclusions representing alternatively pores or accessory minerals [e.g., Jakobsen *et al.*, 2003; Giraud *et al.*, 2007; Cosenza *et al.*, 2008, 2009]. The most popular EMAs such as self-consistent scheme and differential effective medium approach allow to account for various shapes and orientations of inclusions. However, these theoretical works did not consider the spatial clay distribution in clay rocks.

Thus, the main objective of this paper is to quantitatively relate a statistical characterization of the spatial clay distribution and macroscopic electrical property of clay rocks. This quantitative relationship is achieved by revisiting the "Local Porosity Theory" (LPT) [Hilfer, 1991, 1992, 1993, 1996], which offers two advantages: (1) it introduces geometric observables such as the clay fraction and clay connectivity that can be easily measured from mineral maps or images and (2) it can be conveniently used for effective medium calculations of electrical conductivity, as explained further.

A "local clay theory" (LCT), an extension of the LPT, is presented in the first part of the paper. In the second part, it is applied to an accurate mineral map computed from an electron microprobe chemical map [e.g., Prêt *et al.*, 2010a, 2010b] from a COx sample. The results of a direct and inverse modeling are presented in the second part. In the third part, the contributions of this new LCT to the geometric characterization and to the modeling of macroscopic electrical property of clay rocks are presented and discussed.

2. Local Clay Theory

2.1. Geometric Characterization of Clay Rocks

The starting point of our approach is to consider a clay rock as a two-phase medium constituted by a clay phase and a nonclay phase (i.e., accessory minerals). The electrical conductivities of the accessory minerals (quartz and calcite) in the nonclay phase are very low (typically lower than 10^{-3} S m^{-1}) and will be neglected in comparison to that of the clay phase. Moreover, the effect of the largest macropores (whose size may be compared to that of accessory minerals) will be omitted: all pores implied in the electrical transfer mechanisms of clay rock are included in the clay phase. This assumption is also physically reasonable because the amount of

macropores in clay rocks is low and these macropores are unconnected (see, for instance, *Sammartino et al.* [2003] and *Robinet et al.* [2007, 2012]): their contribution to the macroscopic transport will also be neglected in a first-order approach.

Following LPT, we do not try to identify grains, clay aggregates, or other geometrical patterns within the clay rock as the fundamental carrier of randomness but rather the clay fraction itself. More precisely, the clay fraction, ϕ_c , which is the counterpart of the porosity in the LPT, will be considered as a fundamental random variable. This idea leads to the introduction of two quantitative geometric characterizations of clay rocks [Hilfer, 1991, 1996]: local “clay” distributions, named hereafter $\mu(\phi_c)$, and local clay percolation distribution probabilities $\lambda(\phi_c)$. In other words, this approach replaces the characterization of the random microgeometry in terms of clay fraction by these two local functions $\lambda(\phi_c)$ and $\mu(\phi_c)$. This assumption, which is called by Hilfer, the “local simplicity,” offers three advantages: (1) it is generally applicable and mathematically well defined; (2) it is experimentally simpler and more operational than other approaches, which use multiple order correlation functions to describe geometrically heterogeneous media [e.g., *Torquato and Stell*, 1982]; and (3) as explained further, it can be used to easily calculate the effective transport properties. The reader is referred to *Hilfer* [1991, 1992, 1993, 1996] for details.

To define functions $\lambda(\phi_c)$ and $\mu(\phi_c)$, we consider a clay rock sample S (a photograph, a numerical image, or a mineral map), constituted in a clay space C and a solid nonclay space NC (i.e., $S = C \cup NC$). We choose a partitioning $K = \{K_1, \dots, K_j, \dots, K_M\}$ of the sample space S into M mutually disjoint subsets, called measurement cells. As a result, $\cup_{j=1}^M K_j = S$ and $K_i \cap K_j = \emptyset$ if $i \neq j$. Each measurement cell K_j is constituted itself in M_j elementary volume elements. An elementary volume element is the elementary voxel in a 3-D sample or the elementary pixel in a 2-D sample or map.

A particular and simple partitioning K is a cubic lattice for a 3-D sample or a square lattice for a 2-D sample. This choice conveniently features cells K_j that are translated copies of one another and the same set (they all have the same shape). The local clay fraction $\phi_c(K_j)$ inside a measurement cell K_j can be defined as

$$\phi_c(K_j) = \frac{V(C \cap K_j)}{V(K_j)} = \frac{1}{M_j} \sum_{\mathbf{r}_i \in K_j} \chi_c(\mathbf{r}_i) \tag{1}$$

where $V(K_j)$ is the volume of a subset, M_j denotes the number of volume elements (voxels or pixels) in K_j ; χ_c is the characteristic function (indicator function) of clay space C :

$$\chi_c(\mathbf{r}_i) = \begin{cases} 1 & \text{if } \mathbf{r}_i \in C \\ 0 & \text{if } \mathbf{r}_i \notin C \end{cases} \tag{2}$$

From this definition of the local clay fraction $\phi_c(K_j)$, a local clay distribution, $\mu(\phi_c, K)$, can be introduced as follows:

$$\mu(\phi_c, K) = \frac{1}{M \Delta \phi_c} \sum_{j=1}^M \delta(\phi_c - \phi_c(K_j)) \tag{3}$$

where $\delta(x)$ is the Dirac δ distribution which is defined as follows:

$$\delta = \begin{cases} 1 & \text{if } |\phi_c - \phi_c(K_j)| \leq \Delta \phi_c \\ 0 & \text{otherwise} \end{cases} \tag{4}$$

For a given value of ϕ_c , the sum $\sum_{j=1}^M \delta(\phi_c - \phi_c(K_j))$ indicates the number of measurement cells having local clay fraction values included in the interval $(\phi_c, \phi_c + \Delta \phi_c)$. In this way, the parameter $\Delta \phi_c$ defines the interval (of the variable ϕ_c) used to build the histogram associated with the distribution $\mu(\phi_c, K)$. In the practical case of a cubical measurement cell $K_j = K(\mathbf{r}_j, L)$ of side length L centered at the lattice vector \mathbf{r}_j (i.e., typically a Bravais lattice), the local clay distribution can be rewritten as follows:

$$\mu(\phi_c, L) = \frac{1}{M \Delta \phi_c} \sum_{j=1}^M \delta(\phi_c - \phi_c(\mathbf{r}_j, L)) \tag{5}$$

The local clay distribution, $\mu(\phi_c, L)$, has the following physical meaning: it measures the probability to find the local clay fraction ϕ_c between ϕ_c and $\phi_c + d\phi_c$ in a measurement cell of linear dimension L . Thus, this distribution allows to define a mean clay content $\bar{\phi}_c(L)$ as (if $\Delta\phi_c \rightarrow d\phi_c$ with $d\phi_c \ll 1$)

$$\bar{\phi}_c(L) = \int_0^1 \phi_c \mu(\phi_c, L) d\phi_c \quad (6)$$

For a homogeneous clay rock, the mean clay content $\bar{\phi}_c(L)$ is independent of L and

$$\bar{\phi}_c(L) = \phi_c(S) = \frac{V(C)}{V(S)} \quad (7)$$

where the bulk (volumetric) clay content, $\phi_c(S)$, is the ratio of the volume of the clay fraction, $V(C)$, to the volume of the total sample, $V(S)$.

The second geometrical property to characterize local geometry of clay rocks is related to the local connectivity properties of the clay fraction. The local connectivity of clay is a crucial parameter in our approach since the transport of charge carriers (i.e., ions) occurs in the clay phase, i.e., in the porous phase of clay rocks. Let $\lambda(\phi_c, L)$ denotes the fraction of percolating measurement cells of side length L with local clay fraction ϕ_c . The local function $\lambda(\phi_c, L)$ will be called hereafter the “local percolation probability” and is defined as follows:

$$\lambda(\phi_c, L) = \frac{\sum_{j=1}^M \Lambda(\mathbf{r}_j, L) \delta(\phi_c - \phi_c(\mathbf{r}_j, L))}{\sum_{j=1}^M \delta(\phi_c - \phi_c(\mathbf{r}_j, L))} \quad (8)$$

where the indicator function $\Lambda(\mathbf{r}_j, L)$ for the percolation of cell $K(\mathbf{r}_j, L)$ is given by

$$\Lambda(\mathbf{r}_j, L) = \begin{cases} 1 & \text{if } K(\mathbf{r}_j, L) \text{ percolates in all three directions} \\ 0 & \text{otherwise} \dots \end{cases} \quad (9)$$

A measurement cell $K(\mathbf{r}_j, L)$ percolates in the x (y, z , respectively) direction if there exists a path inside the clay phase connecting two faces of the measurement cell that are perpendicular to the x (y, z , respectively) axis. In practice, the function $\Lambda(\mathbf{r}_j, L)$ can be calculated using the Hoshen-Kopelman algorithm [Hoshen and Kopelman, 1976].

From the particular indicator $\Lambda_\alpha(\mathbf{r}_j, L)$ defined by

$$\Lambda_\alpha(\mathbf{r}_j, L) = \begin{cases} 1 & \text{if } K(\mathbf{r}_j, L) \text{ percolates in } \alpha \text{ direction} \\ 0 & \text{otherwise} \dots \end{cases} \quad (10)$$

can be used to calculate the α -direction percolation probability $\lambda_\alpha(\phi_c, L)$:

$$\lambda_\alpha(\phi_c, L) = \frac{\sum_{j=1}^M \Lambda_\alpha(\mathbf{r}_j, L) \delta(\phi_c - \phi_c(\mathbf{r}_j, L))}{\sum_{j=1}^M \delta(\phi_c - \phi_c(\mathbf{r}_j, L))} \quad (11)$$

From equation (8), the total fraction of percolating cells of size L is obtained by integration overall local clay fractions:

$$p(L) = \int_0^1 \mu(\phi_c, L) \lambda(\phi_c, L) d\phi_c \quad (12)$$

The function $p(L)$ characterizes the overall connectivity of the sample at length scale L and is critical for modeling effective properties as explained further.

In summary, the two local functions $\mu(\phi_c, L)$ and $\lambda(\phi_c, L)$ are assumed to constitute an approximate but reasonable geometric characterization of the clay distribution in clay rocks (i.e., the local simplicity assumption). By definition, these functions can be calculated from photographs or numerical images of 2-D thin sections in a fairly straightforward manner.

However, the local functions $\mu(\phi_c, L)$ and $\lambda(\phi_c, L)$ depend a priori on L . As explained by Hilfer [1991], two competing effects should exist. At small L (i.e., L is close to the elementary voxel/pixel size of the image), the local geometries of measurement cells are highly correlated to each other: the local functions $\mu(\phi_c, L)$ and $\lambda(\phi_c, L)$ cannot capture these complex correlations. At large L (i.e., L close to the size of the clay rock sample S), the local

geometries are statistically uncorrelated but each is nearly as complex as the geometry of the full clay distribution of the sample S . This complexity cannot be described by the local clay function ϕ_c and the indicator function for the connectivity $\Lambda(\mathbf{r}_j, L)$ (i.e., the local simplicity assumption fails). Moreover, at large L , in a practical sense, the number of measurement cells may be low affecting the statistical representativeness of functions $\mu(\phi_c L)$ and $\lambda(\phi_c L)$. Consequently, we seek an intermediate and optimal scale, called hereafter the critical length L^* , at which the local geometries are uncorrelated; and on the other hand, the local functions have a sufficiently nontrivial geometric content to reasonably capture the spatial fluctuations of clay content and connectivity. The existence of L^* implies implicitly that the clay rock is assumed to be spatially and statistically homogeneous: the local functions $\mu(\phi_c L)$ and $\lambda(\phi_c L)$ do not depend on the position of the measurement cell.

There exist several candidates for the optimal size L^* [Boger *et al.*, 1992; Biswal *et al.*, 1998; Widjajakusuma *et al.*, 1999, 2003]: the largest grain size, the length scale at the percolation threshold, the two-point correlation length obtained from the clay fraction autocorrelation function, and the percolation length L_p defined from $p(L)$ as follows:

$$\left. \frac{d^2 p}{dL^2} \right|_{L=L_p} = 0 \quad (13)$$

Following LPT and Widjajakusuma *et al.* [2003], the percolation length L_p is the length around which $p(L)$, which is often sigmoidal in shape, changes rapidly from a low value at small L to its trivial value $p(L \rightarrow \infty) = 1$ (if the clay space C is clearly connected at the scale of S). In other words, the condition (13) defines the domain of the transition between local connectivity (at small L) and global connectivity (at large L). Widjajakusuma *et al.* [2003] show that LPT provides a reasonable estimate of the effective permittivity at length L_p .

In the following, the optimal size L^* will be considered equal to the percolation length L_p defined by equation (13). As mentioned by Widjajakusuma *et al.* [2003], this choice offers two advantages: (a) it has been validated for a physical property, i.e., permittivity which is linked, in its complex form, to electrical conductivity (the imaginary part of complex permittivity is directly related to electrical conductivity) and (b) the calculation of L_p is straightforward.

2.2. Effective Medium Calculations of Effective Electrical Conductivity

The main objective of this section is to show how the local functions $\mu(\phi_c, L^*)$ and $\lambda(\phi_c, L^*)$ can be connected to conventional EMAs (Figure 1).

For this purpose, following our modeling approach (i.e., LCT), consider our previous partition of a clay rock sample S : a square lattice of M measurement cells of length L^* for which all measurement cells are statistically independent. To build histograms of local functions $\mu(\phi_c, L^*)$ and $\lambda(\phi_c, L^*)$, k classes of local clay fraction ϕ_c^j ($\phi_c^{j=1}, \dots, \phi_c^{j=k}$) with equal intervals $\Delta\phi_c$ have to be introduced. For each class of value ϕ_c^j , the fraction of percolating (measurement) and nonpercolating (measurement) cells are $\lambda(\phi_c^j, L^*) \mu(\phi_c^j, L^*) \Delta\phi_c$ and $(1 - \lambda(\phi_c^j, L^*)) \mu(\phi_c^j, L^*) \Delta\phi_c$, respectively. For a particular value of ϕ_c^j , the effective property of the conductive fraction and that of the nonconductive (or blocking) fraction is referred as $\sigma_p(\phi_c^j)$ and $\sigma_B(\phi_c^j)$, respectively. Since all measurement cells of length L^* are statistically independent, our clay rock sample S can be considered as a mixture of $2k$ conductive and nonconductive phases associated with the previous k classes of local clay fractions ($\phi_c^{j=1}, \dots, \phi_c^{j=k}$). The conventional EMAs may then be used to this $2k$ phase mixture. For instance, the self-consistent approximation of the effective electrical conductivity σ_{eff} is written as [e.g., Berryman, 1995]

$$\sum_{j=1}^k \left[\lambda(\phi_c^j, L^*) \mu(\phi_c^j, L^*) \Delta\phi_c \frac{\sigma_p(\phi_c^j) - \sigma_{\text{eff}}}{\sigma_p(\phi_c^j) + 2\sigma_{\text{eff}}} + (1 - \lambda(\phi_c^j, L^*)) \mu(\phi_c^j, L^*) \Delta\phi_c \frac{\sigma_B(\phi_c^j) - \sigma_{\text{eff}}}{\sigma_B(\phi_c^j) + 2\sigma_{\text{eff}}} \right] = 0 \quad (14)$$

where parameters $\sigma_p(\phi_c^j)$ and $\sigma_B(\phi_c^j)$ are local effective electrical conductivities of percolating or conducting (index p) and nonpercolating or blocking (index B) measurement cells. The mathematical formulations of $\sigma_p(\phi_c^j)$ and $\sigma_B(\phi_c^j)$ are discussed further.

If $\Delta\phi_c$ tends to zero ($\Delta\phi_c \ll 1$) (increasing the number k accordingly), the Riemann integral formulation proposed by Hilfer is retrieved [Hilfer, 1991, 1996]

$$\int_0^1 \left[\lambda(\phi_c, L^*) \mu(\phi_c, L^*) \frac{\sigma_p(\phi_c) - \sigma_{\text{eff}}}{\sigma_p(\phi_c) + 2\sigma_{\text{eff}}} + (1 - \lambda(\phi_c, L^*)) \mu(\phi_c, L^*) \frac{\sigma_B(\phi_c) - \sigma_{\text{eff}}}{\sigma_B(\phi_c) + 2\sigma_{\text{eff}}} \right] d\phi_c = 0 \quad (15)$$

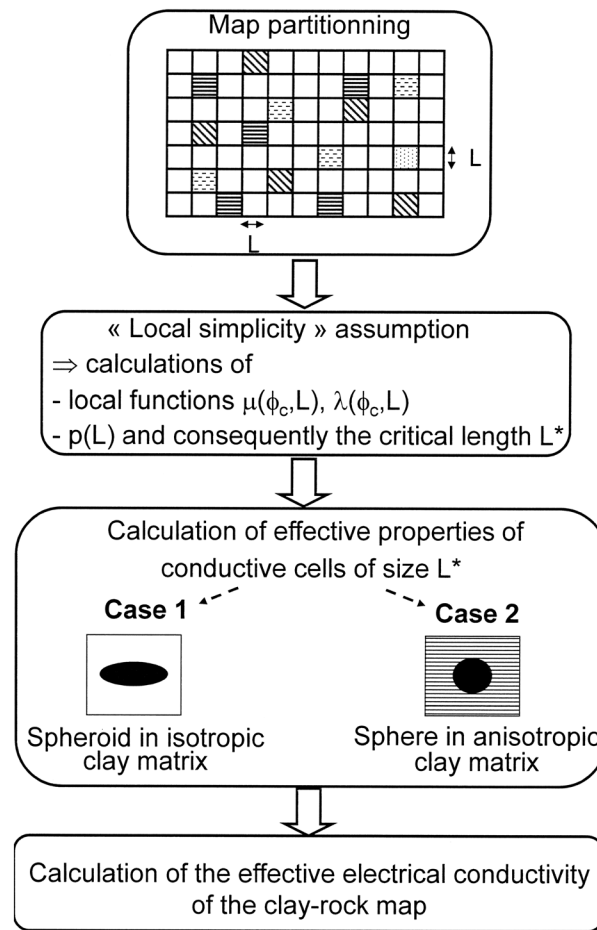


Figure 1. Flowchart of the local clay theory (LCT) used in this work.

Both components σ_{eff}^H and σ_{eff}^V can be independently written because the eigendirections of the effective electrical conductivity tensors of the host medium (i.e., clay matrix) and those of the heterogeneities (i.e., quartz and calcite grains) will be assumed to be parallel in the following (Appendix A) as evidenced by Robinet et al. [2012].

As a matter of fact, equations (14) and (15) have to be rewritten to introduce both parameters σ_{eff}^H and σ_{eff}^V . In case of a self-consistent approximation, the mathematical formulation of effective electrical conductivities of anisotropic mixtures may lead to rather cumbersome integral equations that are complicated to solve. This is why in the following, the differential effective medium (DEM) approach, another conventional EMA, will be preferred since (a) it is easier to implement and (b) it integrates the physical (electromagnetic and mechanical) interactions in a more realistic way than other EMAs (i.e., dilute approximation and Maxwell-Garnett mean field approach).

Moreover, the DEM approach was widely and successfully used in rocks physics in order to model the following properties of sedimentary rocks: (a) elastic properties related to seismic velocities [e.g., Le Ravalec and Guéguen, 1996; Berryman et al., 2002]; (b) DC electrical conductivity [e.g., Sen et al., 1981; Bussian, 1983]; (c) dielectric properties in a wide range of frequencies [e.g., Feng and Sen, 1985; Cosenza et al., 2003; Endres and Bertrand, 2006]; and (d) thermal conductivity [e.g., Revil, 2000]. In comparison with other EMAs, the DEM approach used for modeling effective electromagnetic properties is found to correspond best with experiments involving a large range of geometries and volume fractions [Merrill et al., 1999; Weber et al., 2003].

The DEM approach is fundamentally an iterative process: the effective property of the mixture is explicitly calculated from an initial material through a series of incremental additions of elementary volumes

It should be emphasized that equations (14) and (15) hold for isotropic electrical properties that are not representative of the physical behavior of clay rocks. Indeed, clay rocks are mostly transverse isotropic: they show a rotational symmetry around the axis perpendicular to the bedding planes [e.g., Horseman et al., 1996; Cosenza et al., 2002; Jakobsen et al., 2003; Van Loon et al., 2003, 2004; Giraud et al., 2007; David et al., 2007; Wenk et al., 2007, 2008; Hubert et al., 2013]. The physical properties in all directions parallel to the bedding planes are the same and differ from those perpendicular to the bedding planes. In this case, the anisotropic effective electrical conductivity, $\bar{\sigma}_{\text{eff}}$, is written as follows:

$$\bar{\sigma}_{\text{eff}} = \sigma_{\text{eff}}^H (\bar{e}_x \otimes \bar{e}_x + \bar{e}_y \otimes \bar{e}_y) + \sigma_{\text{eff}}^V (\bar{e}_z \otimes \bar{e}_z) \quad (16)$$

where \otimes : dyadic product (if \bar{a} and \bar{b} are two vectors, the second-order tensor $\bar{a} \otimes \bar{b}$ is defined by $\bar{a} \otimes \bar{b} = a_i b_j$ where a_i and b_j are the Cartesian coordinates of \bar{a} and \bar{b} , respectively); $\bar{e}_x, \bar{e}_y, \bar{e}_z$: vector units in the Cartesian coordinate system; vectors \bar{e}_x, \bar{e}_y are in the horizontal bedding planes, whereas \bar{e}_z is perpendicular to the bedding planes. Both parameters σ_{eff}^H and σ_{eff}^V are the horizontal and the vertical component of the tensor $\bar{\sigma}_{\text{eff}}$, respectively.

(Appendix B). In our case, the procedure begins with the initial material m corresponding to an electrical conductivity, $\bar{\sigma}(\phi_c^{\max}, L^*)$, i.e., the electrical conductivity of conductive measurement cells of local clay fraction ϕ_c^{\max} and of size L^* . The fraction ϕ_c^{\max} is the particular value of ϕ_c corresponding to the highest number of measurement cells of size L^* . The choice of this most conductive fraction as the initial material is classical to model effective electrical conductivity following the DEM scheme [e.g., Mendelson and Cohen, 1982]: in the case of a biphasic rock (typically a saturated sandstone), the starting material in the DEM scheme is the most conductive material, i.e., brine in order to obtain the so-called Archie's law validated experimentally.

In a second step, small volumes of conductive and blocking phases are imbedded in phase m in such a way that the volume remains fixed at V_0 . The effective transport of the mixture is calculated considering a dilute suspension of these small fractions in the medium m . Now, in the volume V_0 , the mixture has a homogenized effective electrical conductivity $\bar{\sigma}_2(L^*)$ and constitutes the initial medium of the next step. The construction process continues such that (a) at each stage, the embedded phases are in dilute concentration and (b) the required volume fractions of conductive and blocking phases are satisfied.

A first-order expansion of a Maxwell-Garnett formulation gives the increment of horizontal electrical conductivity, $\delta\sigma_n^H$, between two steps (step n and step $n - 1$) of the iterative procedure (appendixes A and B):

$$\delta\sigma_n^H = \int_0^1 \left[\lambda(\phi_c, L^*) \mu(\phi_c, L^*) \frac{(\sigma_p^H - \sigma_{n-1}^H) \sigma_{n-1}^H}{\sigma_{n-1}^H + N^H (\sigma_p^H - \sigma_{n-1}^H)} \right] d\phi_c + \int_0^1 \left[(1 - \lambda(\phi_c, L^*)) \mu(\phi_c, L^*) \frac{(\sigma_b^H - \sigma_{n-1}^H) \sigma_{n-1}^H}{\sigma_{n-1}^H + N^H (\sigma_b^H - \sigma_{n-1}^H)} \right] d\phi_c \quad (17)$$

The vertical increment, $\delta\sigma_n^V$, is written in the same way as the horizontal increment $\delta\sigma_n^H$: the superscript H is replaced by the superscript V in equation (17). Equation (17) and its counterpart following the vertical direction have been numerically integrated with a left Riemann rule ($\delta\phi_c = 10^{-5}$) in order to obtain the anisotropic effective electrical conductivity, $\bar{\sigma}_{\text{eff}}$ defined by equation (16).

2.3. Effective Properties of Conductive Cells and Blocking Cells

To use the EMA defined previously, the mathematical formulation of the conductivities of percolating measurement cells, $\bar{\sigma}_p(\phi_c)$ and blocking measurement cells $\bar{\sigma}_b(\phi_c)$ (see equation (17)) must be explicitly addressed (Figure 1).

At this stage, the transport property of blocking cells, $\sigma_b(\phi_c^j)$, is taken equal to zero: this choice leads to mathematical simplification of previous equations (14), (15), and (17).

The conductivities of percolating measurement cells, $\bar{\sigma}_c(\phi_c)$, are modeled by two inclusion-based models, i.e., EMAs (Figure 1): a mixture of aligned isotropic ellipsoids (oblate spheroids) embedded in an isotropic clay matrix (case 1) and a mixture of isotropic spheres embedded in a transversely isotropic clay matrix (case 2). In both cases, the inclusion corresponds to accessory minerals (quartz and calcite grains). These two mixtures are assumed to model the two microstructural origins of the macroscopic anisotropy evidenced by petrographic observations of clay rocks [e.g., Robinet et al., 2007, 2012; David et al., 2007; Wenk et al., 2007, 2008]. In the first mixture, the macroscopic anisotropy is due to aligned spheroidal grains parallel to the bedding planes. In the second mixture, the anisotropy is controlled by that of the clay matrix itself. These two cases are considered separately in the following in order to study their respective contribution on the measured transport properties.

In the first mixture, the spheroidal grains exhibit two horizontal and equal semiprincipal axes ($a_x = a_y$) with respect to the transverse isotropic symmetry of clay rocks. The third semiprincipal axis, a_z , is smaller than the other two to be consistent with petrographic observation. Consequently, spheroidal grains are defined here as oblate spheroids. Moreover, in our calculations, the directions given by the unit vectors \bar{e}_z, \bar{e}_y fixed by the semiprincipal axes a_x and a_y are parallel to the bedding planes. In other words, the principal directions of the spheroidal grains are the same as the principal directions of the effective transport property.

By using again a DEM approach, both components, σ_p^H and σ_p^V , of the tensor $\bar{\sigma}_p(\phi_c)$ can be written as follows (Appendix C):

$$\sigma_p^H = \sigma_c \phi_c^{1/(1-N^H)} \quad (18)$$

$$\sigma_p^V = \sigma_c \phi_c^{1/(1-N^V)} \quad (19)$$

with

$$\bar{\sigma}_p(\phi_c) = \sigma_p^H(\bar{e}_x \otimes \bar{e}_x + \bar{e}_y \otimes \bar{e}_y) + \sigma_p^V(\bar{e}_z \otimes \bar{e}_z) \quad (20)$$

σ_c : the electrical conductivity of the isotropic clay matrix. It should be noted that equations (18) and (19) are mathematically similar to those established by *Mendelson and Cohen* [1982] for aligned spheroidal grains embedded in a interstitial water. The conventional depolarization coefficients N^H and N^V for oblate spheroids are given by [e.g., *Sihvola*, 1999]

$$N^V = \frac{c}{(c-1)^{3/2}} \left(\sqrt{c-1} - \arctan \sqrt{c-1} \right) \quad (21)$$

$$N^H = \frac{1}{2}(1-L^V) \quad (22)$$

where the square of axial ratio c is

$$c = \frac{a_x^2}{a_z^2} \quad (23)$$

As mentioned previously, parameters $a_x(=a_y)$ and a_z are the horizontal semiprincipal axes and the vertical semiprincipal axes of oblate spheroids, respectively.

In the second mixture, the principal axes of the anisotropic clay matrix are the same as the principal axes of the effective transport property. The grains are spheres and of isotropic material. Following *Sihvola* [1999, 2005], both components, σ_p^H and σ_p^V , of the tensor $\bar{\sigma}_p(\phi_c)$ exhibit similar mathematical expressions as previously (Appendix C):

$$\sigma_p^H = \sigma_c^H \phi_c^{1/(1-N^H)} \quad (24)$$

$$\sigma_p^V = \sigma_c^V \phi_c^{1/(1-N^V)} \quad (25)$$

but now, the tensorial electrical conductivity of the anisotropic clay matrix, $\bar{\sigma}_c$, is given by

$$\bar{\sigma}_c = \sigma_c^H(\bar{e}_x \otimes \bar{e}_x + \bar{e}_y \otimes \bar{e}_y) + \sigma_c^V(\bar{e}_z \otimes \bar{e}_z) \quad (26)$$

The modified depolarization coefficients N'^H and N'^V are those of a prolate spheroid:

$$N'^V = \frac{c'}{2(1-c')^{3/2}} \left(\ln \frac{1 + \sqrt{1-c'}}{1 - \sqrt{1-c'}} - 2\sqrt{1-c'} \right) \quad (27)$$

$$N'^H = \frac{1}{2}(1-N'^V) \quad (28)$$

since

$$c' = \frac{\sigma_c^V}{\sigma_c^H} < 1 \quad (29)$$

The condition (29) is introduced to be consistent with experimental observation: the horizontal transport property parallel to the bedding is greater than the vertical transport property [e.g., *Van Loon et al.*, 2003, 2004; *Cosenza et al.*, 2007; *Robinet et al.*, 2007, 2012; *Woodruff et al.*, 2014].

3. Application to Callovo-Oxfordian Mudstone

3.1. Samples Description and Mineral Map

The LCT presented in the previous section and summarized in Figure 1 is now applied to a mineral map made from a Callovo-Oxfordian mudstone.

Table 1. Mineral Composition of the Two Samples Used in This Study [From *Comparison*, 2005]

Depth (m)	Quartz (%)	Carbonates (%)	Clay Minerals (%)	Smectite (%)	Kaolinite (%)	Chlorite (%)	Illite-Smectite (%)
494.76	15	20	65	0	20	30	15

The Callovo-Oxfordian mudstone involved in this study is a clayey formation at the site where the French Meuse/Haute-Marne Underground Research Laboratory has been built. It is a 130 m thick formation of age 150–160 My, located 420–550 m below the surface, in the eastern part of the Paris Basin [Andra, 2005]. The Callovo-Oxfordian formation contains mainly 25 to 65 wt % clay minerals, with 20–42 wt % carbonates (calcite, dolomite, and ankerite) and 15–31 wt % quartz and feldspars [Andra, 2005]. Clay minerals include illite, an illite-smectite mixed layer phase, kaolinite, and chlorite.

The mineral map used in this study was prepared from a drill core, named EST05-709 (–494 m) and retrieved from the Andra EST205 borehole. The rough mineral composition estimated by X-ray diffraction and the petrophysical properties measured in this sample are given in Tables 1 and 2, respectively. The electrical conductivities parallel to the bedding (σ_{exp}^H) and perpendicular to the bedding (σ_{exp}^V) were measured with a two-electrode device at 100 kHz [Comparison, 2005].

The mineral map was obtained at a micrometer spatial resolution from an advanced image processing of a chemical elements map that was acquired through the use of a Cameac SX100 electron probe microanalyzer [Prêt, 2003]. This electron microanalyzer provides quantitative concentration maps of 14 chemical elements (Al, Na, K, Ca, Si, Mg, Ti, Fe, S, Ba, Zr, P, Zn, and Sr) on a $3 \times 0.5 \text{ mm}^2$ area with a spatial resolution of $2 \mu\text{m}/\text{pixel}$. The image processing of these maps is based on mineral thresholding methods that accommodate mixtures and solid solutions. For details, the reader is referred to Prêt [2003] and Prêt *et al.* [2010a, 2010b]. In our case, this methodology allows to locate spatially 16 different minerals including three different clay minerals: illite-smectite mixed layers, kaolinite, and chlorite. No pure illite was detected but two micas are recognized: glauconite and muscovite. The result of this image analysis is given in a numerical file in which the location and mineral code of each pixel of the mineral map are indicated. This numerical file constitutes the input file for calculations of local geometry distributions associated with LCT (see section 3.2).

A region of interest and the properties of the corresponding map are given in Figure 2 and in Table 3, respectively. This map was prepared from a polished thin section in a plane perpendicular to the stratigraphic plane. Thus, the map used in our calculations is strictly 2-D and does not account for the 3-D mineral distribution. The x and y directions indicated in Figure 2 are parallel to the bedding planes, whereas the z direction is perpendicular to the bedding.

The content of a given mineral indicated in Table 3 is the ratio of the number of pixels of the given mineral divided by the total number of pixels. Consequently, Table 3 indicates mineral composition given in terms of “surface” contents (equal to volumetric contents for a Transverse Isotropic (TI) material observed in a plane perpendicular to the stratigraphic plane), whereas mineral contents in Table 2 are expressed in weight percent estimated by processing of X-ray diffraction data. This mainly explains the differences observed between Tables 1 and 3.

3.2. Calculation of the Local Geometry Distributions

The mineral map is now used for calculating the local functions associated with LCT, namely the local clay distribution, $\mu(\phi_c L)$, and the local percolation probabilities, $\lambda(\phi_c L)$, $\lambda_H(\phi_c L)$, $\lambda_V(\phi_c L)$. Figure 3 illustrates these calculations for different sizes of measurement cell L . For the sake of clarity, the histograms have been calculated with a large interval $\Delta\phi_c = 0.02$ and smoothed with a Stineman function [Stineman, 1980]. These local functions, which significantly depend on L , show three significant features.

Table 2. Petrophysical Properties Measured in the Sample EST05-709 Used in This Study [From *Comparison*, 2005]^a

Hg Porosity (%)	CEC (meq/100 g)	Bulk Density (g cm^{-3})	Grain Density (g cm^{-3})	Horizontal Electrical Conductivity σ_{exp}^H (S m^{-1})	Vertical Electrical Conductivity σ_{exp}^V (S m^{-1})
12.4	11.8	2.32	2.66	9.3×10^{-3}	2.8×10^{-3}

^aHg porosity is the porosity measured by mercury intrusion. CEC is the cation exchange capacity expressed per 100 g of rock. Grain density was determined by helium pycnometry. The terms σ_{exp}^H and σ_{exp}^V are horizontal electrical conductivity and vertical electrical conductivity, respectively.

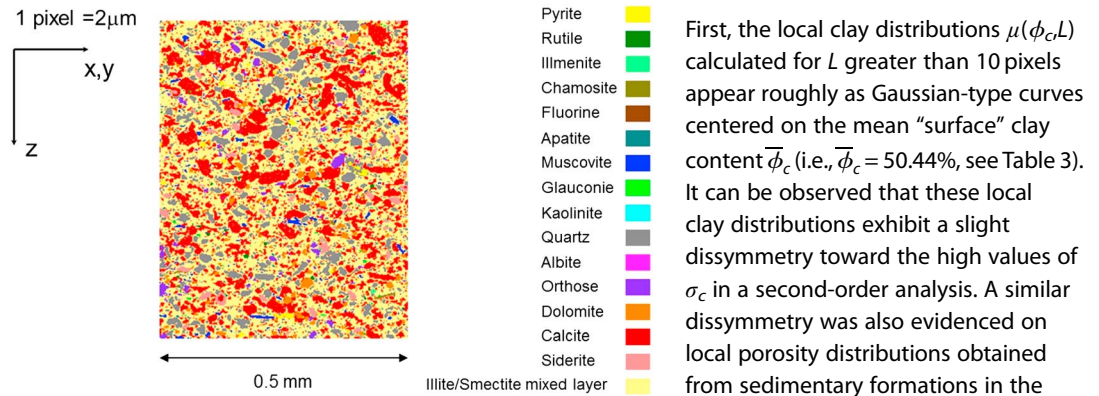


Figure 2. Extraction of the mineral map (sample EST05-709) used in this work.

First, the local clay distributions $\mu(\phi_c L)$ calculated for L greater than 10 pixels appear roughly as Gaussian-type curves centered on the mean “surface” clay content $\bar{\phi}_c$ (i.e., $\bar{\phi}_c = 50.44\%$, see Table 3). It can be observed that these local clay distributions exhibit a slight dissymmetry toward the high values of σ_c in a second-order analysis. A similar dissymmetry was also evidenced on local porosity distributions obtained from sedimentary formations in the framework of the Local Porosity Theory [Widjajakusuma *et al.*, 1999; Boger *et al.*, 1992; Biswal *et al.*, 1998].

Second, the calculated local percolation probabilities $\lambda(\phi_c L)$ and the corresponding connectivities increase with L (Figure 4). Moreover, they show that a minority fraction of measurement cells at the clay fraction $\phi_c = \bar{\phi}_c$ percolates. In other words, all the measurement cells percolate (i.e., $\lambda = 1$) for ϕ_c values of considerably greater than the mean value $\bar{\phi}_c$ calculated from the mineral map.

Third, Figure 5 indicates that for this sample and whatever the value of L , the horizontal probability values are greater than the vertical probability values with distributions simply shifted: the connectivity of this sample is better in the direction parallel to the bedding planes. In this case, the anisotropy of connectivity is controlled by the preferential orientation of nonclayey grains following the direction of bedding. This feature, which is not clearly observable in the mineral map, confirms previous studies [e.g., Robinet *et al.*, 2007, 2012; David *et al.*, 2007] and justifies the reliability of case 1 in our modeling approach (i.e., isolated and aligned spheroids in isotropic clay matrix; see Figure 1). This anisotropy of connectivity should induce an anisotropy of effective electrical conductivity.

To calculate the effective electrical conductivity of this mineral map, the total fractions of percolating cells $\rho(L)$ and the corresponding critical length L^* have to be determined. Following the results given in Figure 6, three domains can be identified. The first domain (Domain 1) is associated with a “local” connectivity (length sizes less than 40 pixels). In this domain, the total fraction of percolating cells increases significantly with L . The domain of large values of L (Domain 3) is related to a “global” connectivity of measurement cells whose length sizes, greater than 75 pixels, are close in dimension to that of the mineral map. Between these domains, the intermediate domain 2 exhibits a plateau for which the criterion defined by equation (13) can be satisfied. As a result and from criterion (13), a critical length L^* of 55 ± 5 pixels is estimated (Figure 6).

This estimation with the EMAs described previously can be used to model effective electrical conductivity.

3.3. Direct and Inverse Modeling

On the basis of the linear equations involved in the DEM scheme, it is easy to note that for both mixture cases considered in our modeling approach, the following linear relationships are satisfied:

Case 1 (mixture of aligned spheroids in an isotropic clay matrix)

$$\sigma_{\text{eff}}^H \propto \sigma_c \quad \text{and} \quad \sigma_{\text{eff}}^V \propto \sigma_c \quad (30)$$

or

$$\sigma_{\text{eff}}^H = f_H \left(\frac{a_x}{a_z}, L^* \right) \sigma_c \quad \text{and} \quad \sigma_{\text{eff}}^V = f_V \left(\frac{a_x}{a_z}, L^* \right) \sigma_c \quad (31)$$

Table 3. Geometrical and Mineralogical Features of the Mineral Map Used in This Work

Resolution (μm)	Total Number of Pixels	Dimensions (Pixels)	Dimensions (μm)	Clay Minerals (%)	Quartz (%)	Calcite (%)
2	384 000	250 × 1536	500 × 3072	50.44	13.83	24.99

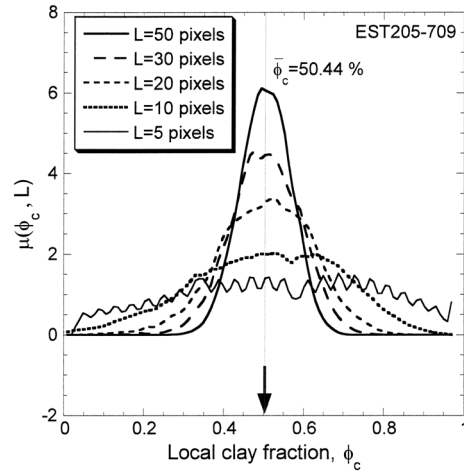


Figure 3. Local clay distribution, $\mu(\phi_c, L)$, calculated for different sizes of measurement cell L .

where σ_c : the electrical conductivity of the isotropic clay matrix; f_H and f_V : functions of a_x/a_z and L^* .

Case 2 (mixture of spheres in an anisotropic clay matrix)

$$\sigma_{\text{eff}}^H \propto \sigma_c^H \quad \text{and} \quad \sigma_{\text{eff}}^V \propto \sigma_c^V \quad (32)$$

or

$$\sigma_{\text{eff}}^H = g_H \left(\frac{\sigma_c^H}{\sigma_c^V}, L^* \right) \sigma_c^H \quad \text{and} \quad \sigma_{\text{eff}}^V = g_V \left(\frac{\sigma_c^H}{\sigma_c^V}, L^* \right) \sigma_c^V \quad (33)$$

where σ_c^H (σ_c^V respectively): the horizontal (vertical respectively) component of the tensorial electrical conductivity of the anisotropic clay matrix; g_H and g_V : functions of σ_c^H/σ_c^V and L^* .

For case 1, relationships (31) lead to

$$\frac{\sigma_{\text{eff}}^H}{\sigma_{\text{eff}}^V} = \frac{f_H \left(\frac{a_x}{a_z}, L^* \right)}{f_V \left(\frac{a_x}{a_z}, L^* \right)} = f \left(\frac{a_x}{a_z}, L^* \right) \quad (34)$$

This equation means that at a given L^* , the effective conductivity ratio, $\sigma_{\text{eff}}^H/\sigma_{\text{eff}}^V$, only depends on the ratio of semiprincipal axes of oblate spheroids (a_x/a_z).

For case 2, relationships (33) yield

$$\frac{\sigma_{\text{eff}}^H}{\sigma_{\text{eff}}^V} = \frac{\sigma_c^H g_H \left(\frac{\sigma_c^H}{\sigma_c^V}, L^* \right)}{\sigma_c^V g_V \left(\frac{\sigma_c^H}{\sigma_c^V}, L^* \right)} = \frac{\sigma_c^H}{\sigma_c^V} g \left(\frac{\sigma_c^H}{\sigma_c^V}, L^* \right) \quad (35)$$

For this case, at a given L^* , the effective conductivity ratio, $\sigma_{\text{eff}}^H/\sigma_{\text{eff}}^V$, only depends on the matrix conductivity ratio, $1/c' = \sigma_c^H/\sigma_c^V$ (the parameter c' was introduced in section 2.3, see equation (29)).

Consequently, from (34) and (35), at a given L^* , the effective conductivity ratios of both cases only depend on a single parameter (a_x/a_z or σ_c^H/σ_c^V), respectively; thus, these ratios can be simply plotted on the same figure (Figure 7).

By considering a critical length of L^* of 55 pixels (see section 3.2), Figure 7 shows that the effective conductivity ratio is more sensitive to changes in axes ratio of nonclay grains than to changes in matrix conductivity ratio. A multiplication of the effective conductivity ratio by a factor 4 requires a multiplication by a factor 4.1 of the axes ratio and by a factor 5.7 of the matrix conductivity ratio. This difference in sensitivity and curve shape can be explained by the mathematical formulation of depolarization coefficients used in the calculations of the effective properties of conductive cells (compare equations (21) and (27)).

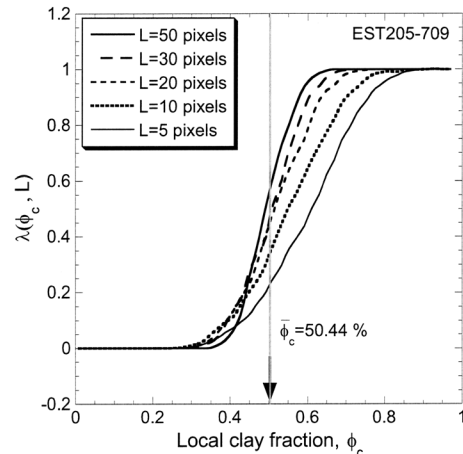


Figure 4. Local percolation probability, $\lambda(\phi_c, L)$, calculated for different sizes of measurement cell L .

As illustrated in Figure 7, the univoque relationships between the effective conductivity ratio and the microstructural ratios (a_x/a_z and σ_c^H/σ_c^V) can be also used to invert the microstructural parameters of both mixture models describing the percolating measurement cells. If we assume a statistical homogeneity at the EST05-709 sample scale, i.e.,

$$\sigma_{\text{eff}}^H = \sigma_{\text{exp}}^H \quad \text{and} \quad \sigma_{\text{eff}}^V = \sigma_{\text{exp}}^V \quad (36)$$

where the electrical conductivity measurements σ_{exp}^H and σ_{exp}^V are given in Table 2, microstructural parameters

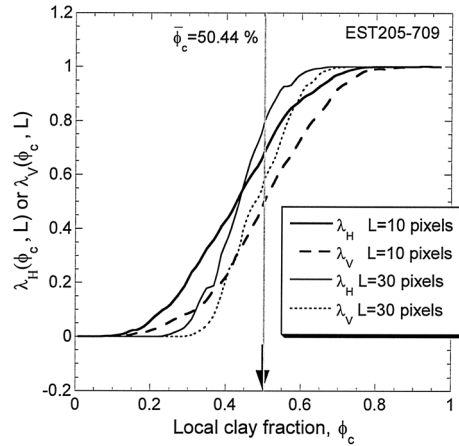


Figure 5. Horizontal and vertical local percolation probabilities, $\lambda_H(\phi_c, L)$ and $\lambda_V(\phi_c, L)$, calculated for different sizes of measurement cell L .

determined from the functions f_H , f_V (case 1), g_H , and g_V (case 2). Since these functions are independent of clay conductivities (σ_c , σ_c^H , and σ_c^V), they are obtained from linear equations (31) and (33) in particular cases, i.e., at $\sigma_c = \sigma_c^H = \sigma_c^V = 1 \text{ S m}^{-1}$, as explained below.

Case 1: The horizontal effective conductivity estimated at $\sigma_c = 1 \text{ S m}^{-1}$, namely $\sigma_{\text{eff}, \sigma_c=1}^H$, and the vertical effective conductivity estimated at $\sigma_c = 1 \text{ S m}^{-1}$, $\sigma_{\text{eff}, \sigma_c=1}^V$, are introduced from (31):

$$\sigma_{\text{eff}, \sigma_c=1}^H = f_H \left(\frac{a_x}{a_z}, L^* \right) \times 1 \quad (39)$$

$$\sigma_{\text{eff}, \sigma_c=1}^V = f_V \left(\frac{a_x}{a_z}, L^* \right) \times 1 \quad (40)$$

From (39), (40), and (31), f_H and f_V are given by

$$f_H \left(\frac{a_x}{a_z}, L^* \right) = \frac{\sigma_{\text{eff}, \sigma_c=1}^H}{1} = \frac{\sigma_{\text{exp}}^H}{\sigma_c} \quad (41)$$

$$f_V \left(\frac{a_x}{a_z}, L^* \right) = \frac{\sigma_{\text{eff}, \sigma_c=1}^V}{1} = \frac{\sigma_{\text{exp}}^V}{\sigma_c} \quad (42)$$

And finally, from (41) and (42), the isotropic clay conductivity, σ_c , is given by

$$\sigma_c = \frac{\sigma_{\text{exp}}^H}{\sigma_{\text{eff}, \sigma_c=1}^H} \times 1 = \frac{\sigma_{\text{exp}}^H}{\sigma_{\text{eff}, \sigma_c=1}^H} \quad (43)$$

or

$$\sigma_c = \frac{\sigma_{\text{exp}}^V}{\sigma_{\text{eff}, \sigma_c=1}^V} \times 1 = \frac{\sigma_{\text{exp}}^V}{\sigma_{\text{eff}, \sigma_c=1}^V} \quad (44)$$

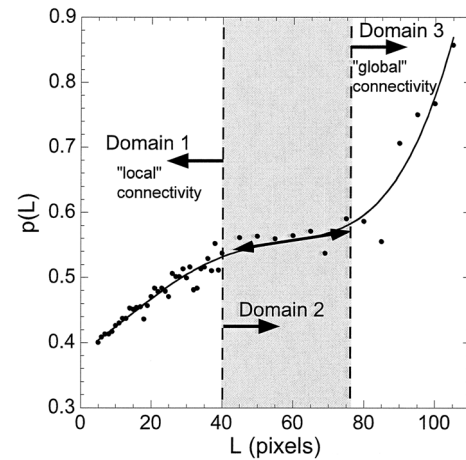


Figure 6. The total fraction of percolating cells of size L , $p(L)$. For the sake of clarity, a polynomial fit is also indicated. To use the criterion (13), the tangent crossing the curve at the inflection point is drawn.

The parameters $\sigma_{\text{eff}, \sigma_c=1}^H$ and $\sigma_{\text{eff}, \sigma_c=1}^V$ are calculated following the DEM scheme described in sections 2.2 and 2.3 (formally written by equation (31)) by considering $\sigma_c = 1 \text{ S m}^{-1}$ and the value of axes ratio, a_x/a_z , calculated from the first step.

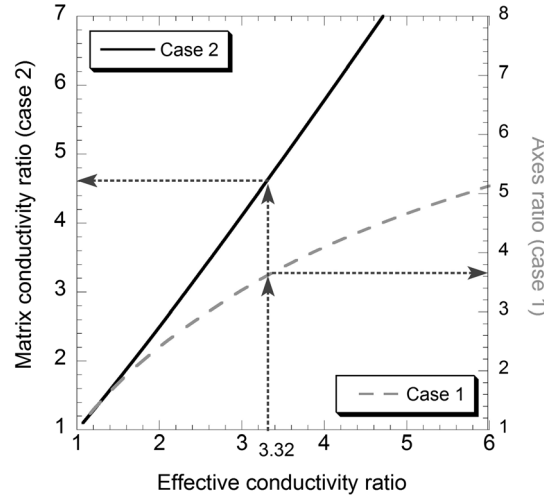


Figure 7. Matrix conductivity ratio (case 1) σ_c^H/σ_c^V and axes ratio (case 2) a_x/a_z versus effective conductivity ratio. The experimental value of effective conductivity ratio (3.32) is also indicated. Grey arrows give the estimations of matrix conductivity ratio and axes ratio used in this work.

Case 2: Following the same idea, the horizontal effective conductivity estimated at $\sigma_c^H = 1 \text{ S m}^{-1}$, namely $\sigma_{\text{eff},\sigma_c^H=1}^H$, and the vertical effective conductivity estimated at $\sigma_c^V = 1 \text{ S m}^{-1}$, $\sigma_{\text{eff},\sigma_c^V=1}^V$, are introduced from (33):

$$\sigma_{\text{eff},\sigma_c^H=1}^H = g_H \left(\frac{\sigma_c^H}{\sigma_c^V}, L^* \right) \times 1 \quad (45)$$

$$\begin{aligned} \sigma_{\text{eff},\sigma_c^V=1}^V &= g_V \left(\frac{\sigma_c^H}{\sigma_c^V}, L^* \right) \times \sigma_c^V \\ &= g_V \left(\frac{\sigma_c^H}{\sigma_c^V}, L^* \right) \times c' \times \sigma_c^H \\ &= g_V \left(\frac{\sigma_c^H}{\sigma_c^V}, L^* \right) \times c' \times 1 \end{aligned} \quad (46)$$

Parameter $1/c'$ is the known matrix conductivity ratio σ_c^H/σ_c^V which is calculated from the first step.

From (45), (46), and (33), g_H and g_V are given by

$$g_H \left(\frac{\sigma_c^H}{\sigma_c^V}, L^* \right) = \frac{\sigma_{\text{eff},\sigma_c^H=1}^H}{1} = \frac{\sigma_{\text{exp}}^H}{\sigma_c^H} \quad (47)$$

$$g_V \left(\frac{\sigma_c^H}{\sigma_c^V}, L^* \right) = \frac{\sigma_{\text{eff},\sigma_c^V=1}^V}{c' \times 1} = \frac{\sigma_{\text{exp}}^V}{\sigma_c^V} \quad (48)$$

Finally, from (47) and (48), the tensorial components, σ_c^H and σ_c^V are calculated by

$$\sigma_c^H = \frac{\sigma_{\text{exp}}^H \times 1}{\sigma_{\text{eff},\sigma_c^H=1}^H} = \frac{\sigma_{\text{exp}}^H}{\sigma_{\text{eff},\sigma_c^H=1}^H} \quad (49)$$

$$\sigma_c^V = \frac{\sigma_{\text{exp}}^V \times c' \times 1}{\sigma_{\text{eff},\sigma_c^V=1}^V} = \frac{\sigma_{\text{exp}}^V \times c'}{\sigma_{\text{eff},\sigma_c^V=1}^V} \quad (50)$$

The $\sigma_{\text{eff},\sigma_c^H=1}^H$ and $\sigma_{\text{eff},\sigma_c^V=1}^V$ are calculated following the DEM scheme described in sections 2.2 and 2.3 (formally written by equation (33)) by considering $\sigma_c^H = \sigma_c^V = 1 \text{ S m}^{-1}$ and the value of the matrix conductivity ratio, $\sigma_c^H/\sigma_c^V (= 1/c')$, obtained from the first step.

By considering the estimated range of L^* (i.e., 55 ± 5 pixels), the final results obtained from this inversion scheme are given in Table 4. They show that the inverted microstructural parameters, i.e., σ_c , a_x/a_z , σ_c^H , and σ_c^V are slightly dependent on L^* .

4. Discussion

4.1. Microstructural Origins of the Anisotropy in Electrical Conductivity

If the statistical homogeneity implied in (34) is valid, one may wonder if the inverted values of both mixture models (cases 1 and 2) can provide some physical insights into the origins of the anisotropy in electrical conductivity measured in clay rocks. To answer to this question, we propose to compare the inverted values of both model mixtures with those expected from the literature.

If the sole microstructural ratios a_x/a_z and σ_c^H/σ_c^V are considered, the inverted values obtained in Table 4 are consistent with previous petrophysical and petrographic studies. Petrographic observations performed in

Table 4. Inverted Values of Microstructural Parameters Obtained From LCT ($L^* = 50, 55,$ and 60 Pixels) and the Mean Clay Model^a

$L^* = 50$ Pixels				$L^* = 55$ Pixels				$L^* = 60$ Pixels				Mean Clay Model			
Case 1		Case 2		Case 1		Case 2		Case 1		Case 2		Case 1		Case 2	
a_x/a_z	σ_c	σ_c^H	σ_c^V	a_x/a_z	σ_c	σ_c^H	σ_c^V	a_x/a_z	σ_c	σ_c^H	σ_c^V	a_x/a_z	σ_c	σ_c^H	σ_c^V
3.59	2.07	2.91	0.61	3.67	1.97	2.75	0.59	4.11	1.83	2.47	0.55	3.34	2.12	3.03	0.63
± 0.005	± 0.005	± 0.005	± 0.005	± 0.005	± 0.005	± 0.005	± 0.005	± 0.005	± 0.005	± 0.005	± 0.005	± 0.005	± 0.005	± 0.005	± 0.005

^aAll the conductivity values (σ_c , and σ_c^V) are expressed in 10^{-2} S m^{-1} . Both inclusion-based models in LCT are considered (case 1: aligned spheroids in an isotropic clay matrix; case 2: spheres in a transverse isotropic clay matrix).

the COx mudstone [Jorand, 2006; Robinet et al., 2007, 2012] have shown that the axes ratios of the accessory minerals (carbonates and quartz) were mainly in the range of 1.3–4. The inverted values of a_x/a_z , close to 3.7 (Table 4), are a little high in comparison with the average of the previous range but they do not contradict fundamentally the previous petrographic observations. Concerning the ratio σ_c^H/σ_c^V of pure and saturated clayey materials, experimental data are scarce in literature but Mousseau and Trump [1967] and Comparon [2005] reported values in the range of 1.1–25.5, obtained in compacted and saturated kaolinite and bentonite samples. This range of values includes our inverted values of σ_c^H/σ_c^V .

The values of conductivities σ_c and σ_c^H fall in the range of 2×10^{-2} – 10 (S m^{-1}) obtained from studies performed on pure clayey systems [e.g., Cremers and Laudelout, 1965; Weiler and Chaudisson, 1968; Revil et al., 1998; Saarenketo, 1998; Tabbagh and Cosenza, 2007]. However, the value of σ_c^V (about $6 \times 10^{-3} \text{ S m}^{-1}$) appears to be too low for pure clayey materials: it is likely unrealistic for a pure clay matrix. This discrepancy may have petrophysical and theoretical origins.

The petrophysical origins include a small desaturation of the sample after its recovery and the existence of a microscopic and nonclayey phase hidden in the clay matrix. Considering the latter, small amounts of calcite cements known as isolating electrical materials may have precipitated in the microporosity associated with the clay matrix [e.g., Buschaert et al., 2004] inducing a lower electrical conductivity.

However, some theoretical bias associated with our modeling process cannot be excluded. The first bias is obvious: this modeling approach is based on a 2-D information (a mineral map), whereas electrical measurements imply 3-D tortuous paths of charge carriers. Moreover, though our approach accounts for local fluctuations of clay phase and connectivity, it does not integrate the spatial variability and hence the distribution of (a) orientations and elongations of nonclayey particles and that of (b) the ratios a_x/a_z and σ_c^H/σ_c^V . Indeed, these microstructural features may have significant and nonlinear impacts of the macroscopic electrical conductivity [e.g., Mendelson and Cohen, 1982; Sen, 1997]. The estimation of these effects will be the purpose of a future work.

Summarizing the confrontation between the inverted values in Table 4 and those given in literature shows that the simplified and usual picture proposed in the model case 2 (i.e., spherical nonclayey grains in a transverse isotropic clay matrix) cannot solely explain the anisotropy in the measured electrical conductivity. In contrast to the usual belief that the anisotropy of transport properties is mainly controlled by the anisotropy of the clay matrix [e.g., Van Loon et al., 2004; Motellier et al., 2007], our results confirm that others candidates, for instance, the anisotropy induced by elongated and oriented nonclayey grains, should be considered.

However, this conclusion is clearly associated with the choice of two basic morphological units or inclusion-based models (i.e., case 1 and case 2 in Figure 1) and one may wonder if more classical EMAs, which would not account for local fluctuations of clay content and connectivity, would have provide the same qualitative results. This question is addressed in the following section.

4.2. Impact of the Local Fluctuations of Clay Content and Connectivity on the Macroscopic Conductivity

In order to study the sole impact of local fluctuations of clay content and connectivity on the macroscopic conductivity, the results from LCT and those obtained from a DEM rule using the sole mean value $\bar{\phi}_c$ ($\bar{\phi}_c = 50.44\%$, see Table 3) are compared. The latter model is called the “mean clay model” in the following.

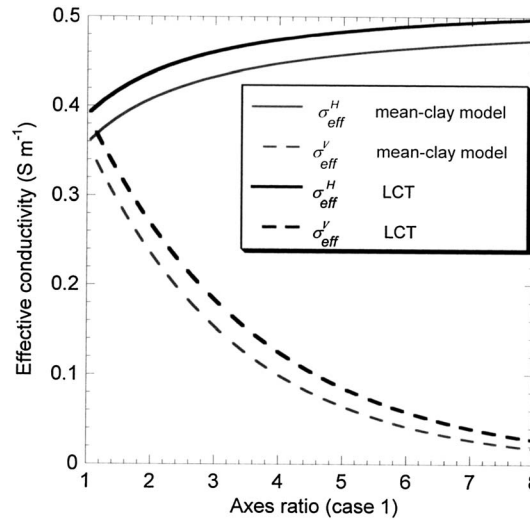


Figure 8. Vertical (σ_{eff}^V) and Horizontal (σ_{eff}^H) components of the effective conductivity tensor calculated from the mean clay model and LCT as a function of the axes ratio (case 1).

(case 2, Figure 9). These values are of the same order of magnitude as those inverted previously in section 3.3 (see Table 4).

Figures 8 and 9 show that the effective conductivities calculated by LCT are systematically greater than those obtained from the mean clay model. In other words, for the same values of microstructural parameters, if the local fluctuations of clay content and connectivity are considered, the effective medium appears more conductive than that with a mean clay fraction $\bar{\phi}_c$.

This result can be explained if the local functions $\mu(\phi_c L^*)$ and $\lambda(\phi_c L^*)$ are both taken into account (Figure 10). For the mean value $\phi_c = 50.44\%$, Figure 10 shows that less than 55% of the measurement cells percolate (see the vertical arrow in Figure 10). The greatest value of clay fraction for which the fraction of percolating cells is maximum is indicated in Figure 10 by a circle: it is greater than 50.44% and close to the value of 55%. In other words, for the same microstructural parameters, the effective medium sees a clay fraction

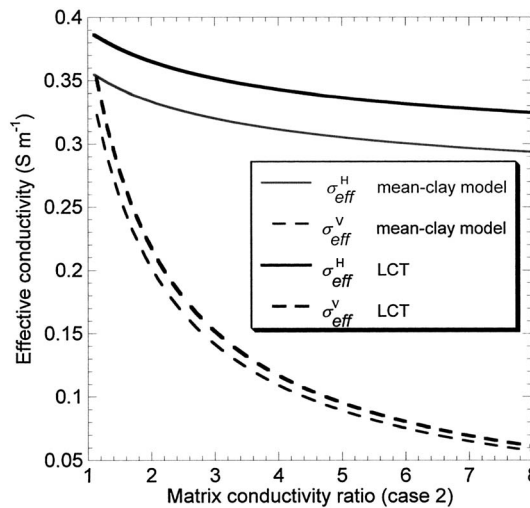


Figure 9. Vertical (σ_{eff}^V) and horizontal (σ_{eff}^H) components of the effective conductivity tensor calculated from the mean clay model and LCT as a function of the matrix conductivity ratio (case 2).

For case 1, the effective conductivity of the mean clay model can be written as follows:

$$\bar{\sigma}_{eff} = \sigma_c \bar{\phi}_c^{1/(1-N^H)} (\bar{e}_x \otimes \bar{e}_x + \bar{e}_y \otimes \bar{e}_y) + \sigma_c \bar{\phi}_c^{1/(1-N^V)} (\bar{e}_z \otimes \bar{e}_z) \quad (51)$$

where the conventional depolarization coefficients N^H and N^V for oblate spheroids are given by equations (21) and (22).

For case 2, it yields

$$\bar{\sigma}_{eff} = \sigma_c^H \bar{\phi}_c^{1/(1-N'^H)} (\bar{e}_x \otimes \bar{e}_x + \bar{e}_y \otimes \bar{e}_y) + \sigma_c^V \bar{\phi}_c^{1/(1-N'^V)} (\bar{e}_z \otimes \bar{e}_z) \quad (52)$$

where the modified depolarization coefficients N'^H and N'^V are expressed in (27) and (28).

The results obtained from LCT and the mean clay model are displayed in Figures 8 and 9. It should be noted that these calculations were performed with $\sigma_c = 1 \text{ S m}^{-1}$ (case 1, Figure 8) and $\sigma_c^H = 1 \text{ S m}^{-1}$

contributing significantly to the effective conductivity, considerably greater than the mean clay fraction $\bar{\phi}_c$ of 50.44%. Since the effective conductivity is an increasing function of clay fraction, ϕ_c , the effective conductivity will be greater when the local functions $\mu(\phi_c L^*)$ and $\lambda(\phi_c L^*)$ are considered.

However, if the microstructural parameters of the mean clay model (for both mixture cases) are now inverted, the results given in Table 4 seem to contradict the previous statement: the conductivity values of the clay matrix associated with the mean clay model are significantly lower than those given by LCT. This apparent contradiction can be understood as a consequence of two effects (Figure 11).

First, considering case 1, the mean clay model shows lower values of a_x/a_z than those calculated from LCT. To compensate this effect, the clay conductivity σ_c has to increase.

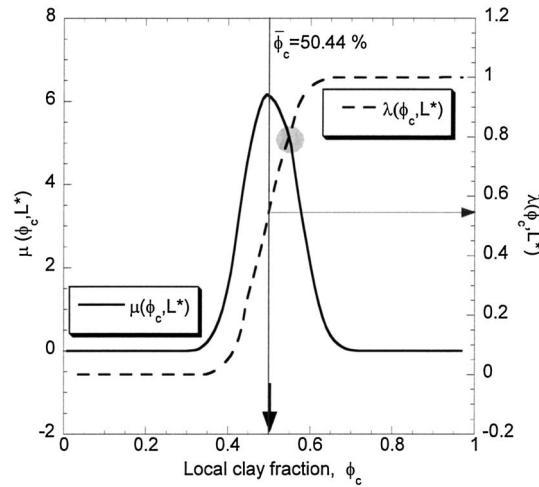


Figure 10. Local clay distribution, $\mu(\phi_c L^*)$, and local percolation probability, $\lambda(\phi_c L^*)$, as a function of local clay fraction. L^* is taken equal to 55 pixels. The circle indicates an optimum clay fraction of percolating measurement cells.

parameters (Table 4): the differences between the inverted values of the mean clay model and that of LCT are less than 15%.

5. Conclusion

This work introduced a LCT to establish a quantitative relationship between the effective (macroscopic) electrical conductivity and the clay distribution of clay rocks. This theory is based on three assumptions. First, a clay rock can be considered as a two-phase medium composed of a clay and a nonclay phases. Second, a local simplicity assumption implies that the complexity of spatial clay distribution can be captured by two local functions $\mu(\phi_c L)$ and $\lambda(\phi_c L)$ calculated from a partitioning of a mineral map (L : the map side length) and a local clay fraction ϕ_c of each subset called measurement cell. The local clay distribution $\mu(\phi_c L)$ provides information about spatial clay fluctuations, and the local percolation probabilities $\lambda(\phi_c L)$ describe spatial connectivity fluctuations. Third, there exists a side length L^* for which the local geometries given by local functions $\mu(\phi_c L^*)$ and $\lambda(\phi_c L^*)$ in each measurement cells are uncorrelated with each other. This assumption allows for the connection of both local functions for EMAs (here, a DEM scheme).

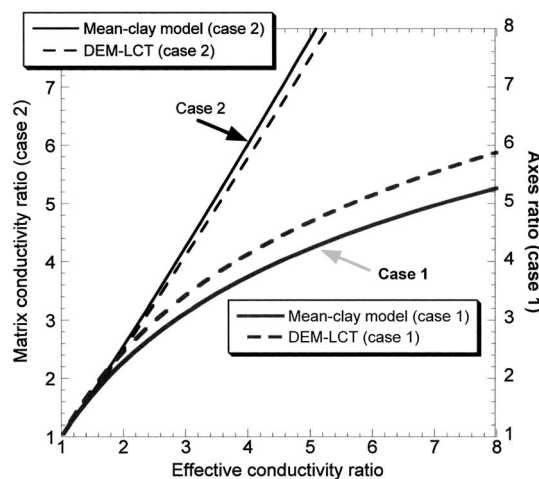


Figure 11. Matrix conductivity ratio (case 1), σ_c^H/σ_c^V , and axes ratio (case 2) a_x/a_z as a function of effective conductivity ratio for two models: mean clay model and DEM-LCT.

Second, considering case 2, the mean clay model leads to greater values of σ_c^H/σ_c^V than those obtained from LCT. This results from an increase of both clay conductivities σ_c^H and σ_c^V .

Consequently, these results confirmed two important features of our modeling approach. On the one hand, the effective conductivity is not only governed by that of the clay matrix: the microstructural ratios, a_x/a_z and σ_c^H/σ_c^V , play an important role. On the other hand, effective conductivity mainly depends of the choice of morphological units in the inclusion-based models (i.e., aligned spheroids in an isotropic clay matrix and spheres in an anisotropic clay matrix) included in the DEM scheme. In comparison with the mean field approach associated with DEM, the introduction of local fluctuations of clay content and connectivity does not modify the order of magnitude of the inverted values of microstructural

This LCT was applied to (a) a mineral map made from a Callovo-Oxfordian mudstone sample and (b) electrical conductivity measurements performed on the same sample. This application shows three results.

First, the horizontal probability values are greater than the vertical probability values: the connectivity of this sample is better in the direction parallel to the bedding planes. In this case, the anisotropy of connectivity is controlled by the preferential orientation of nonclay grains following the direction of bedding.

Second, the textural and classical model assuming that the anisotropy is mainly controlled by the anisotropy of the clay matrix provides inconsistent inverted values of the clay vertical conductivity. On the basis of this result and the previous calculations of the percolation

probabilities, our approach suggests that the anisotropy induced by elongated and oriented nonclayey grains should be considered.

Third, the effective conductivity values obtained from this LCT primarily depend on the choice of the morphological units implied in EMAs. The local fluctuations of clay content and connectivity slightly modify the modeling results.

These modeling results suggest the need for further investigations in two directions. First, this work has accounted for simple microstructural patterns but can be extended by incorporating additional microscopic features (e.g., orientation of nonclay grains) that would have been quantified [e.g., *Robinet et al.*, 2012]. Thus, this work confirms the interest of microstructural investigations and mapping techniques to identify the microscopic and geometric factors controlling the effective properties measured in the field. Second, this LCT which can be seen an easy-to-use model in comparison with other numerical approaches should be tested for other transport properties (e.g., diffusion coefficient or thermal conductivity).

Appendix A: Effective Transport Coefficient of an Anisotropic Mixture of Anisotropic Spherical Inclusions—The Maxwell-Garnett Scheme

In this section, the results obtained from the Maxwell-Garnett scheme are presented. They are essential in our approach since they will be used to establish the mathematical formulation of the effective electrical conductivity, $\bar{\sigma}_{\text{eff}}$ following the DEM scheme (Appendix B).

Consider a mixture of n anisotropic spherical inclusions of radius a in an anisotropic host medium. In the case of the static limit (i.e., at very low angular frequencies, $\omega \rightarrow 0$), the Maxwell-Garnett rule allows to obtain the effective electrical conductivity of this mixture, $\bar{\sigma}_{\text{eff}}$, a second-order tensor, as follows [*Sihvola*, 1996, 1999]:

$$\bar{\sigma}_{\text{eff}} = \bar{\sigma}_e + \left[\bar{1} - \bar{\sigma}_e^{-1} \bar{N}' \sum_{j=1}^n \bar{\beta}_j \right]^{-1} \sum_{j=1}^n \bar{\beta}_j \tag{A1}$$

with

$$\bar{\beta}_j = f_j (\bar{\sigma}_j - \bar{\sigma}_e) \left[\bar{\sigma}_e + \bar{N}' (\bar{\sigma}_j - \bar{\sigma}_e) \right]^{-1} \bar{\sigma}_e \tag{A2}$$

where $\bar{\sigma}_e$: the electrical conductivity tensor of the host medium; f_j : the volumetric fraction of spherical inclusions j ; $\bar{\sigma}_j$: the electrical conductivity tensor of the spherical inclusions j ; and \bar{N}' : the modified depolarization tensor [*Sihvola*, 1999]:

$$\bar{N}' = \frac{\det \bar{A}}{2 \int_0^{\infty} ds \bar{\sigma}_e \frac{\left(\frac{-s^2}{\bar{A} + s \bar{\sigma}_e} \right)^{-1}}{\sqrt{\det(\bar{A}^2 + s \bar{\sigma}_e)}}} \tag{A3}$$

where \bar{A} is a symmetric and positive-definite second-order tensor given by

$$\bar{A} = \sum_{i=x,y,z} a \bar{e}_i \otimes \bar{e}_i \tag{A4}$$

with a : radius of the spherical inclusions, $\bar{e}_x, \bar{e}_y, \bar{e}_z$: vector units in the Cartesian coordinate system, and \otimes : dyadic product. The tensor \bar{A} also obeys to the following property:

$$\det \bar{A} = a^3 \tag{A5}$$

In case of a transverse isotropic material for which the eigendirections of both tensors, $\bar{\sigma}_e$ and $\bar{\sigma}_j$, are parallel

$$\bar{\sigma}_e = \sigma_e^H (\bar{e}_x \otimes \bar{e}_x + \bar{e}_y \otimes \bar{e}_y) + \sigma_e^V (\bar{e}_z \otimes \bar{e}_z) \tag{A6}$$

$$\bar{\sigma}_j = \sigma_j^H (\bar{e}_x \otimes \bar{e}_x + \bar{e}_y \otimes \bar{e}_y) + \sigma_j^V (\bar{e}_z \otimes \bar{e}_z) \tag{A7}$$

The horizontal component, σ_{eff}^H , and the vertical component, σ_{eff}^V , of the effective electrical conductivity, $\bar{\sigma}_{\text{eff}}$, given in (A1) can be simplified as follows:

$$\sigma_{\text{eff}}^H = \sigma_e^H + \frac{\sum_{j=1}^n \beta_j^H}{1 - \frac{N^H}{\sigma_e^H} \sum_{j=1}^n \beta_j^H} \quad (\text{A8})$$

$$\sigma_{\text{eff}}^V = \sigma_e^V + \frac{\sum_{j=1}^n \beta_j^V}{1 - \frac{N^V}{\sigma_e^V} \sum_{j=1}^n \beta_j^V} \quad (\text{A9})$$

with

$$\beta_j^X = \frac{f_j (\sigma_j^X - \sigma_e^X) \sigma_e^X}{\sigma_e^X + L^X (\sigma_j^X - \sigma_e^X)} \quad (X = H \text{ or } V) \quad (\text{A10})$$

and [e.g., *Sihvola, 2005*]

$$N^{jV} = \frac{1 - e^2}{2e^3} \left(\ln \frac{1 + e}{1 - e} - 2e \right) \quad (\text{A11})$$

with

$$e = \sqrt{1 - \frac{\sigma_e^V}{\sigma_e^H}} \quad (\text{if } \sigma_e^V < \sigma_e^H) \quad (\text{A12})$$

$$N^H = \frac{1 - N^{jV}}{2} \quad (\text{A13})$$

Here it should be noted that the horizontal direction corresponds to that of the bedding planes.

In the framework of our modeling approach (i.e., LCT), consider a clay rock sample S as a mixture of $2k$ conductive and nonconductive phases associated with k classes of local clay fractions ($\phi_c^{j=1}, \dots, \phi_c^{j=k}$). On the basis of the previous equations, the Maxwell-Garnett rule allows to write the effective electrical conductivity, $\bar{\sigma}_{\text{eff}}$, as follows:

$$\bar{\sigma}_{\text{eff}} = \sigma_{\text{eff}}^H (\bar{e}_x \otimes \bar{e}_x + \bar{e}_y \otimes \bar{e}_y) + \sigma_{\text{eff}}^V (\bar{e}_z \otimes \bar{e}_z) \quad (\text{A14})$$

where the horizontal component, σ_{eff}^H , is now given by

$$\sigma_{\text{eff}}^H = \sigma^H(\phi_c^{\text{max}}, L^*) + \frac{\sum_{j=1}^{k-1} \beta_j^P(\phi_c^j, \phi_c^{\text{max}}, L^*) + \sum_{j=1}^k \beta_j^B(\phi_c^j, \phi_c^{\text{max}}, L^*)}{1 - \frac{N^H}{\sigma^H(\phi_c^{\text{max}}, L^*)} \left(\sum_{j=1}^{k-1} \beta_j^P(\phi_c^j, \phi_c^{\text{max}}, L^*) + \sum_{j=1}^k \beta_j^B(\phi_c^j, \phi_c^{\text{max}}, L^*) \right)} \quad (\text{A15})$$

with

$$\beta_j^P = \frac{f_j^P \left[\sigma_{P,j}^H(\phi_c^j, L^*) - \sigma^H(\phi_c^{\text{max}}, L^*) \right] \sigma^H(\phi_c^{\text{max}}, L^*)}{\sigma_{P,j}^H(\phi_c^j, L^*) + N^H \left[\sigma_{P,j}^H(\phi_c^j, L^*) - \sigma^H(\phi_c^{\text{max}}, L^*) \right]} \quad (\text{A16})$$

$$\beta_j^B = \frac{f_j^B \left[\sigma_{B,j}^H(\phi_c^j, L^*) - \sigma^H(\phi_c^{\text{max}}, L^*) \right] \sigma^H(\phi_c^{\text{max}}, L^*)}{\sigma_{B,j}^H(\phi_c^j, L^*) + N^H \left[\sigma_{B,j}^H(\phi_c^j, L^*) - \sigma^H(\phi_c^{\text{max}}, L^*) \right]} \quad (\text{A17})$$

The $\sigma^H(\phi_c^{\text{max}}, L^*)$: the horizontal electrical conductivity of conductive measurement cells of size L^* and of local clay fraction ϕ_c^{max} . The value ϕ_c^{max} is the particular value of ϕ_c corresponding to the highest number of measurement cells of size L^* (i.e., the highest value of ϕ_c^j among the k classes of local clay fraction $\phi_c^{j=1}, \dots, \phi_c^{j=k}$). Following this choice, the class of cells of local clay fraction ϕ_c^{max} is considered as a host medium.

The parameters f_j^P and f_j^B are the fraction of percolating (measurement) cells (i.e., $\lambda(\phi_c^j, L^*) \mu(\phi_c^j, L^*) \Delta \phi_c$) and the fraction of nonpercolating (measurement) cells (i.e., $(1 - \lambda(\phi_c^j, L^*)) \mu(\phi_c^j, L^*) \Delta \phi_c$), for each class of local

clay fraction ϕ_c^j , respectively. The parameter $\sigma_{p,j}^H(\phi_c^j, L^*)$ (respectively $\sigma_{B,j}^H(\phi_c^j, L^*)$) is the horizontal electrical conductivity of percolating (respectively, blocking) cells of size L^* and clay fraction ϕ_c^j . The modified depolarization coefficient N^{H} is given by the equations (A11), (A12), and (A13).

The vertical component, σ_{eff}^V , is written in the same way: the superscript H is replaced by the superscript V in equations (A15), (A16), and (A17).

Appendix B: Effective Electrical Conductivity of an Anisotropic Mixture of Anisotropic Spherical Inclusions—The Differential Effective Medium Rule

Following an iterative process, the effective property of the mixture is explicitly calculated from an initial material through a series of incremental additions of elementary volumes. The procedure begins with the initial material m corresponding to an electrical conductivity $\bar{\sigma}(\phi_c^{\text{max}}, L^*)$, i.e., the electrical conductivity of conductive measurement cells of local clay fraction ϕ_c^{max} and of size L^* . As previously, the value ϕ_c^{max} defines the particular value of ϕ_c corresponding to the highest number of measurement cells of size L^* .

Small volumes of $(k - 1)$ conductive phases and $(k - 1)$ blocking phases are imbedded in phase m in such a way that the volume remains fixed at V_0 . The $(k - 1)$ conductive phases and the $(k - 1)$ blocking phases are associated with the electrical conductivities $\bar{\sigma}_{p,j}(\phi_c^j, L^*)$ (with $j = 1, \dots, k - 1$) and $\bar{\sigma}_{B,j}(\phi_c^j, L^*)$ (with $j = 1, \dots, k - 1$), respectively. The effective transport of the mixture is calculated considering a dilute suspension of these 2 $(k - 1)$ small volumes in the medium m : the volumetric fractions f_j^p , (with $j = 1, \dots, k - 1$) and f_j^B , (with $j = 1, \dots, k - 1$) in equations (A15) and (A16) (and their counterpart following the vertical direction) are replaced by $\delta V_j^p / V_0$ and $\delta V_j^B / V_0$, respectively. Now, in the volume V_0 , the mixture has a homogenized effective electrical conductivity $\bar{\sigma}_2(L^*)$ and constitutes the initial medium of the next step. The construction process continues such that (a) at each stage, the embedded phases are in dilute concentration and (b) the required volume fractions f_j^p (with $j = 1, \dots, k - 1$) and f_j^B (with $j = 1, \dots, k - 1$) are satisfied.

By replacing in the Maxwell-Garnett equations (A15) and (A16), the parameters σ_{eff}^H , $\sigma^H(\phi_c^{\text{max}}, L^*)$, f_j^p , and f_j^B by σ_n^H , σ_{n-1}^H , $\delta V_j^p / V_0$ ($\ll 1$), and $\delta V_j^B / V_0$ ($\ll 1$), respectively, a first-order expansion of equation (A15) gives the increment of horizontal conductivity, $\delta \sigma_n^H$, between two steps (step n and step $n - 1$) of the iterative procedure:

$$\delta \sigma_n^H = \sum_{j=1}^{k-1} \frac{\frac{\delta V_j^p}{V_0} (\sigma_{j,p}^H - \sigma_{n-1}^H) \sigma_{n-1}^H}{\sigma_{n-1}^H + N^{H} (\sigma_{j,p}^H - \sigma_{n-1}^H)} + \sum_{j=1}^k \frac{\frac{\delta V_j^B}{V_0} (\sigma_{j,B}^H - \sigma_{n-1}^H) \sigma_{n-1}^H}{\sigma_{n-1}^H + N^{H} (\sigma_{j,B}^H - \sigma_{n-1}^H)} \quad (\text{B1})$$

where parameters σ_n^H and σ_{n-1}^H are the horizontal effective property at step n and the horizontal effective property at step $n - 1$, respectively; parameter $\sigma_{j,p}^H$ (respectively $\sigma_{j,B}^H$) is the horizontal conductivity of the percolating (resp., blocking) phase j ; parameter δV_j^p (respectively δV_j^B) is the volumetric increment of the percolating (respectively blocking) phase j .

Due to the high number of phases in the mixture, the overlapping between inclusions of phase j and those of phase l ($l \neq j$) is neglected in the construction process. Consequently, the “incompressibility” assumption recommended by Norris [1985] leads to

$$\frac{\delta V_j^p}{V_0} = \frac{\delta f_j^p}{1 - f_j^p} = \lambda(\phi_c^j, L^*) \mu(\phi_c^j, L^*) \frac{\delta \phi_c}{1 - \lambda(\phi_c^j, L^*) \mu(\phi_c^j, L^*) \delta \phi_c} \quad (\text{B2})$$

$$\frac{\delta V_j^B}{V_0} = \frac{\delta f_j^B}{1 - f_j^B} = (1 - \lambda(\phi_c^j, L^*)) \mu(\phi_c^j, L^*) \frac{\delta \phi_c}{1 - (1 - \lambda(\phi_c^j, L^*)) \mu(\phi_c^j, L^*) \delta \phi_c} \quad (\text{B3})$$

If $\delta \phi_c$ tends to zero ($\delta \phi_c \ll 1$) in equations (B1), (B2), and (B3), equation (B1) can be written as follows:

$$\delta \sigma_n^H = \int_0^1 \left[\lambda(\phi_c, L^*) \mu(\phi_c, L^*) \frac{(\sigma_p^H - \sigma_{n-1}^H) \sigma_{n-1}^H}{\sigma_{n-1}^H + N^{H} (\sigma_p^H - \sigma_{n-1}^H)} \right] d\phi_c + \int_0^1 \left[(1 - \lambda(\phi_c, L^*)) \mu(\phi_c, L^*) \frac{(\sigma_B^H - \sigma_{n-1}^H) \sigma_{n-1}^H}{\sigma_{n-1}^H + N^{H} (\sigma_B^H - \sigma_{n-1}^H)} \right] d\phi_c \quad (\text{B4})$$

where the first integral in the right member of equation (B4) can be considered here as an improper Riemann integral since its calculation excludes the local clay fraction ϕ_c^{\max} for which the associated electrical conductivity was calculated separately for the initial material:

$$\int_0^1 f(\phi_c) d\phi_c = \lim_{\varepsilon \rightarrow 0^+} \int_0^{\phi_c^{\max} - \varepsilon} f(\phi_c) d\phi_c + \lim_{\varepsilon \rightarrow 0^-} \int_{\phi_c^{\max} + \varepsilon}^1 f(\phi_c) d\phi_c \quad (B5)$$

with

$$f(\phi_c) = \lambda(\phi_c, L^*) \mu(\phi_c, L^*) \frac{(\sigma_p^H - \sigma_{n-1}^H) \sigma_{n-1}^H}{\sigma_{n-1}^H + N^H (\sigma_p^H - \sigma_{n-1}^H)} \quad (B6)$$

The vertical increment, $\delta\sigma_n^V$, is written in the same way: the superscript H is replaced by the superscript V in equation (B4).

Appendix C: Differential Effective Medium Schemes for the Electrical Conductivities of Conductive Measurement Cells

First, consider the simplest mixture: aligned prolate spheroids of transport property σ_i embedded in an isotropic host medium with transport property being σ_e . Note that in our case, the spheroids are aligned parallel to the bedding planes.

The Maxwell-Garnett formula for the two components of the effective electrical conductivity of this mixture is [e.g., *Sihvola, 1999*]:

$$\sigma_{\text{eff}}^H = \sigma_e + f \sigma_e \frac{\sigma_i - \sigma_e}{\sigma_e + (1 - f) N^H (\sigma_i - \sigma_e)} \quad (C1)$$

$$\sigma_{\text{eff}}^V = \sigma_e + f \sigma_e \frac{\sigma_i - \sigma_e}{\sigma_e + (1 - f) N^V (\sigma_i - \sigma_e)} \quad (C2)$$

where f is the volumetric fraction of spheroids; N^H and N^V are the conventional depolarization factors. If the semi-axes of the prolate spheroid in three orthogonal directions are a_x , a_y , and a_z , the conventional depolarization factors are given by

$$N^V = \frac{c}{2(1 - c)^{3/2}} \left(\ln \frac{1 + \sqrt{1 - c}}{1 - \sqrt{1 - c}} - 2\sqrt{1 - c} \right) \quad (C3)$$

$$N^H = \frac{1}{2} (1 - N^V) \quad (C4)$$

where the axial ratio c is

$$c = \frac{a_x^2}{a_z^2} \quad (C5)$$

For instance, if we focused on the horizontal component σ_e^H , the equation (C1) can be also given the form

$$\frac{\sigma_{\text{eff}}^H / \sigma_e - 1}{\sigma_{\text{eff}}^H / \sigma_e + u} = f \frac{\sigma_i / \sigma_e - 1}{\sigma_i / \sigma_e + u} \quad (C6)$$

with $u = (1 - N^H) / N^H$ being a coefficient that depends on the shape of the spheroid.

In the framework of a DEM scheme, the volumetric fraction f , the parameters σ_i and σ_e are replaced in (C1) by the parameters $\delta V / V_0$, σ_n^H , and σ_{n-1}^H , respectively:

$$\frac{\delta\sigma^H}{\delta\sigma^H + (1 + u)\sigma_{n-1}^H} = \frac{\delta V}{V_0} \frac{\sigma_i - \sigma_{n-1}^H}{\sigma_i + u\sigma_{n-1}^H} \quad (C7)$$

where parameters σ_n^H ($\sigma_n^H = \sigma_{n-1}^H + \delta\sigma^H$) and σ_{n-1}^H are the horizontal effective property at step n and the horizontal effective property at step $n - 1$, respectively; δV is an infinitesimal increment of volume of spheroidal inclusions; V_0 is the volume of the mixture (held constant in the construction process). Since the spheroidal grains are made of isolated material (quartz or calcite) ($\sigma_i = 0$), a first-order expansion of equation (C4)

gives the increment of horizontal electrical conductivity, $\delta\sigma_n^H$, between two steps (step n and step $n - 1$) of the iterative procedure:

$$\frac{\delta\sigma_n^H}{(1+u)\sigma_{n-1}^H} = \frac{\delta V}{V_0} \left(-\frac{1}{u} \right) \quad (C8)$$

In the construction process associated with the DEM scheme, the volume of the mixture is held constant (i.e., $V = V_0$): at each replacement, the removed material must have the same volume fraction of material. This “incompressibility” assumption leads to the following condition [e.g., Norris, 1985]:

$$\frac{\delta V}{V_0} = \frac{\delta f}{1-f} \quad (C9)$$

Now, the differential equation (C4) can be written as follows:

$$\frac{\delta\sigma_n^H}{(1+u)\sigma_{n-1}^H} = \frac{\delta f}{1-f} \left(-\frac{1}{u} \right) \quad (C10)$$

By integrating (C10) from $\sigma_{n-1}^H = \sigma_c$ and $f=0$ to $\sigma_{n-1}^H = \sigma^H$ and $f=f_c = 1 - \phi_c$, the following equation is obtained:

$$\sigma^H = \sigma_c \phi_c^{(1+u)/u} = \sigma_c \phi_c^{1/(1-N^H)} \quad (C11)$$

A similar formulation can be obtained for vertical effective property σ^V (the horizontal depolarization factor N^H is replaced by its vertical counterpart N^V in equation (C8)).

In the second mixture used to calculate the electrical conductivities of conductive measurement cells, the anisotropy is controlled by that of the clay matrix itself: a mixture of isotropic spheres embedded in a transversely isotropic clay matrix is now considered. Furthermore, it is assumed that (a) the grains are spheres and of isotropic material and (b) the principal axes of the anisotropic clay matrix are the same as the principal axes of the effective electrical conductivity. In this case, the tensorial electrical conductivity of the anisotropic host medium (i.e., clay matrix), $\bar{\sigma}_e$, is given by

$$\bar{\sigma}_e = \sigma_e^H (\bar{e}_x \otimes \bar{e}_x + \bar{e}_y \otimes \bar{e}_y) + \sigma_e^V (\bar{e}_z \otimes \bar{e}_z) \quad (C12)$$

where, as previously, the directions given by the unit vectors \bar{e}_x, \bar{e}_y are parallel to the bedding planes. Following a Maxwell-Garnett rule, the two components of the effective medium are given by *Sihvola* [1999, 2005]:

$$\sigma_{\text{eff}}^H = \sigma_e^H + f \sigma_e^H \frac{\sigma_i - \sigma_e^H}{\sigma_e^H + (1-f)N^H(\sigma_i - \sigma_e^H)} \quad (C13)$$

$$\sigma_{\text{eff}}^V = \sigma_e^V + f \sigma_e^V \frac{\sigma_i - \sigma_e^V}{\sigma_e^V + (1-f)N^V(\sigma_i - \sigma_e^V)} \quad (C14)$$

where the modified depolarization factors N^H and N^V depend on both components σ_e^H and σ_e^V via the uniaxiality c' given by

$$c' = \frac{\sigma_e^V}{\sigma_e^H} \quad (C15)$$

If $c' < 1$

$$N^V = \frac{c'}{2(1-c')^{3/2}} \left(\ln \frac{1 + \sqrt{1-c'}}{1 - \sqrt{1-c'}} - 2\sqrt{1-c'} \right) \quad (C16)$$

If $c' > 1$

$$N^V = \frac{c'}{(c'-1)^{3/2}} \left(\sqrt{c'-1} - \arctan \sqrt{c'-1} \right) \quad (C17)$$

In both cases

$$N^H = \frac{1}{2} (1 - N^V) \quad (C18)$$

Equation (C14) is similar to equation (C1) except that σ_e is replaced by σ_e^H . Consequently, the same procedure similar to the first mixture can be used to obtain

$$\sigma^H = \sigma_e^H \phi_c^{1/(1-N^H)} \quad (C19)$$

The vertical component, σ^V , is written in the same way: the superscript H is replaced by the superscript V in equation (C19).

Acknowledgments

We thank the French National Agency for Radioactive Waste Management (Andra) (specially P. Lebon, J.-C. Robinet, and P. Landrein) and TAPSS 2000 research program (Present and past transfers in a sedimentary aquifer-aquitard system: a 2000 m deep drill hole in the Mesozoic of the Paris Basin) and NEEDS-MIPOR for their financial supports. The data, i.e., the mineral map presented in Figure 2, are available from the authors upon request.

References

- Andra (2005), Dossier 2005 Argile: Synthèse, évaluation de la faisabilité d'un dépôt géologique en formation argilieuse, Andra, France. [Available at www.andra.fr.]
- Berryman, J. G. (1995), Mixture theories for rock properties, in *Rock Physics and Phase Relations: A Handbook of Physical Constants*, edited by T. J. Arhens, pp. 205–228, AGU, Washington, D. C.
- Berryman, J. G., S. R. Pride, and H. F. Wang (2002), A differential scheme for elastic properties of rocks with dry and saturated cracks, *Geophys. J. Int.*, *151*, 597–611.
- Biswal, B., C. Manwart, and R. Hilfer (1998), Three dimensional local porosity analysis of porous media, *Phys. A*, *255*, 221.
- Boger, F., J. Feder, T. Jossang, and R. Hilfer (1992), Microstructural sensitivity of local porosity distributions, *Phys. A*, *187*, 55–70.
- Buschaert, S., S. Fourcade, M. Cathelineau, E. Deloube, F. Martineau, M. Ayt Ougougdal, and A. Trouiller (2004), Widespread cementation induced by inflow of continental water in the eastern part of the Paris basin: O and C isotopic study of carbonate cements, *Appl. Geochem.*, *19*(8), 1201–1215.
- Bussian, A. E. (1983), Electrical conductance in a porous medium, *Geophysics*, *48*(9), 1258–1268.
- Coelho, D., J.-F. Thovert, and P. M. Adler (1997), Geometrical and transport properties of random packings of spheres and aspherical particles, *Phys. Rev. E*, *55*, 1959–1978.
- Comparon, L. (2005), Etude expérimentale des propriétés et diélectriques des matériaux argileux consolidés, PhD thesis, Institut de Physique du Globe de Paris.
- Cosenza, P., M. Ghoreychi, G. de Marsily, G. Vasseur, and S. Violette (2002), Theoretical prediction of poroelastic properties of argillaceous rocks from in situ specific storage coefficient, *Water Resour. Res.*, *38*(10), 1207, doi:10.1029/2001WR001201.
- Cosenza, P., C. Camerlynck, and A. Tabbagh (2003), Differential effective medium schemes for investigating the relationship between high frequency relative dielectric permittivity and water content of soils, *Water Resour. Res.*, *39*(9), 1230, doi:10.1029/2002WR001774.
- Cosenza, P., A. Ghorbani, N. Florsch, and A. Revil (2007), Effects of drying on the low-frequency electrical properties of Tournemire argillites, *Pure Appl. Geophys.*, *164*(10), 2043–2066.
- Cosenza, P., A. Ghorbani, A. Revil, M. Zamora, M. Schmutz, D. Jougnot, and N. Florsch (2008), A physical model of the low-frequency electrical polarization of clay-rocks, *J. Geophys. Res.*, *113*, B08204, doi:10.1029/2007JB005539.
- Cosenza, P., A. Ghorbani, C. Camerlynck, F. Rejiba, R. Guérin, and A. Tabbagh (2009), Effective medium theories for modeling the relationships between electromagnetic properties and hydrological variables: A review, *Near Surf. Geophys.*, *7*(3), 563–578, doi:10.3997/1873-0604.2009009.
- Cremers, A., and H. Laudelout (1965), Conductivité électrique des gels argileux et anisométrie de leurs éléments, *J. Chem. Phys.*, *62*, 1155–1161.
- David, C., P. Robion, and B. Menendez (2007), Anisotropy of elastic, magnetic and microstructural properties of the Callovo-Oxfordian argillite, *Phys. Chem. Earth*, *32*, 145–153.
- Endres, A. L., and E. A. Bertrand (2006), A pore size scale model for the dielectric properties of water saturated clean rocks and soils, *Geophysics*, *75*, F185–F193.
- Feng, S., and P. N. Sen (1985), Geometrical model of conductive and dielectric properties of partially saturated rocks, *J. Appl. Phys.*, *58*(8), 3236–3243.
- Giraud, A., C. Gruescu, D. P. Do, F. Homand, and D. Kondo (2007), Effective thermal conductivity of transversely isotropic media with arbitrary oriented ellipsoidal inhomogeneities, *Int. J. Solids Struct.*, *44*, 2627–2647.
- Hilfer, R. (1991), Geometric and dielectric characterization of porous media, *Phys. Rev. B*, *44*(1), 60–75.
- Hilfer, R. (1992), Local-porosity theory for flow in porous media, *Phys. Rev. B*, *45*(13), 7115–7121.
- Hilfer, R. (1993), Local porosity theory for electrical and hydrodynamical transport through porous media, *Phys. A*, *194*, 406–414.
- Hilfer, R. (1996), Transport and relaxation phenomena in porous media, in *Advances in Chemical Physics*, edited by I. Prigogine and S. T. Rice, pp. 299–424, John Wiley, New York.
- Horseman, S. T., J. J. W. Higgo, J. Alexander, and J. F. Harrington (1996), Water, gas and solute movement through argillaceous media, *Nuclear Energy Agency Rep. CC-96/1*, OECD, Paris.
- Hoshen, J., and R. Kopelman (1976), Percolation and cluster distribution. I. Cluster multiple labeling technique and critical concentration algorithm, *Phys. Rev. B*, *1*(14), 3438–3445.
- Hubert, F., I. Bihannic, D. Prêt, E. Tertre, B. Nauleau, M. Pelletier, B. Demé, and E. Ferrage (2013), Investigating the anisotropic features of particle orientation in synthetic swelling clay porous media, *Clays Clay Miner.*, *61*(5), 397–415.
- Jakobsen, M., J. A. Hudson, and T. A. Johansen (2003), T-matrix approach to shale acoustics, *Geophys. J. Int.*, *154*, 533–558.
- Jorand, R. (2006), Etude expérimentale de la conductivité thermique: Application au forage EST205 du site de Meuse/Haute Marne (ANDRA), PhD thesis, Univ. of Denis Diderot, Paris.
- Jougnot, D., A. Revil, and P. Leroy (2009), Diffusion of ionic tracers in the Callovo-Oxfordian clay-rock using the Donnan equilibrium model and the formation factor, *Geochim. Cosmochim. Acta*, *73*, 2712–2726.
- Jougnot, D., A. Ghorbani, A. Revil, P. Leroy, and P. Cosenza (2010), Spectral induced polarization of partially saturated clay-rocks: A mechanistic approach, *Geophys. J. Int.*, *180*(1), 210–224.

- Keller, L. M., L. Holzer, R. Wepf, and P. Gasser (2011), 3D geometry and topology of pore pathways in Opalinus clay: Implications for mass transport, *Appl. Clay Sci.*, *52*, 85–95.
- Le Ravalec, M., and Y. Guéguen (1996), High- and low-frequency elastic moduli for saturated porous/cracked rock-Differential self-consistent and poroelastic theories, *Geophysics*, *61*(4), 1080–1094.
- Leroy, P., and A. Revil (2009), A mechanistic model for the spectral induced polarization of clay materials, *J. Geophys. Res.*, *114*, B10202, doi:10.1029/2008JB006114.
- Mendelson, K. S., and M. H. Cohen (1982), The effect of grain anisotropy on the electrical properties of sedimentary rocks, *Geophysics*, *47*, 257–263.
- Merrill, M. W., R. E. Diaz, M. M. LoRe, M. Squires, and M. C. Alexopoulos (1999), Effective medium theories for artificial materials composed of multiple sizes of spherical inclusions in a host continuum, *IEEE Trans. Antennas Propag.*, *47*(1), 142–147.
- Motellier, S., I. Devol-Brown, S. Savoye, D. Thoby, and J.-C. Alberto (2007), Evaluation of tritiated water diffusion through the Toarcian clayey formation of the Tournemire experimental site (France), *J. Contam. Hydrol.*, *94*(1–2), 99–108.
- Mousseau, R. J., and R. P. Trump (1967), Measurement of electrical anisotropy of clay-like materials, *J. Appl. Phys.*, *38*(11), 4375–4379.
- Norris, A. N. (1985), A differential scheme for the effective moduli of composites, *Mech. Mater.*, *4*, 1–16.
- Paszakuta, M., M. Rosanne, and P. M. Adler (2006), Transport coefficients of saturated compact clays, *C. R. Geosci.*, *338*, 908–916.
- Prêt, D. (2003), Nouvelles méthodes quantitatives de cartographie de la minéralogie et de la porosité dans les matériaux argileux: Application aux bentonites compactées des barrières ouvragées, 257 pp., Univ. of Poitiers, France.
- Prêt, D., S. Sammartino, D. Beaufort, A. Meunier, M. Fialin, and L. Michot (2010a), A new method for quantitative petrography based on image processing of chemical elements maps: Part I. Mineral mapping applied to compacted bentonites, *Am. Mineral.*, *95*, 1379–1388.
- Prêt, D., S. Sammartino, D. Beaufort, M. Fialin, P. Sardini, P. Cosenza, and A. Meunier (2010b), A new method for quantitative petrography based on image processing of chemical elements maps: Part II. Semi-quantitative porosity maps superimposed on mineral maps, *Am. Mineral.*, *95*, 1389–1398.
- Pusch, R. (2006), Clays and nuclear waste management, in *Handbook of Clay Science*, Developments in Clay Science, edited by F. Bergaya, B. K. G. Theng, and G. Lagaly, pp. 703–716, Elsevier, Amsterdam, Netherlands.
- Revil, A. (2000), Thermal conductivity of unconsolidated sediments with geophysical applications, *J. Geophys. Res.*, *105*(B7), 16,749–16,768, doi:10.1029/2000JB900043.
- Revil, A., and N. Florsch (2010), Determination of permeability from spectral induced polarization in granular media, *Geophys. J. Int.*, *181*, 1480–1498.
- Revil, A., L. M. Cathles III, S. Losh, and J. A. Nunn (1998), Electrical conductivity in shaly sands with geophysical applications, *J. Geophys. Res.*, *103*(B10), 925–936.
- Revil, A., W. Woodruff, C. Torres-Verdín, and M. Prasad (2013), Complex conductivity tensor of anisotropic hydrocarbon-bearing shales and mudrocks, *Geophysics*, *78*(6), D403–D418.
- Robinet, J. C., D. Prêt, P. Sardini, and D. Coelho (2007), Solute diffusion in Bure argillite at millimeter to micrometer scales: The role of mineral and microstructural heterogeneities, 3rd Annual Workshop Proceedings, 6th EC FP – FUNMIG IP, Edinburgh, 26th–29th Nov.
- Robinet, J. C., P. Sardini, D. Coelho, J. C. Parneix, D. Prêt, S. Sammartino, and S. Altmann (2012), Effects of mineral distribution at mesoscopic scale on solute diffusion in a clay-rich rock: Example of the Callovo-Oxfordian mudstone (Bure, France), *Water Resour. Res.*, *48*, W05554, doi:10.1029/2011WR011352.
- Saarenketo, T. (1998), Electrical properties of water in clay and silty soils, *J. Appl. Geophys.*, *40*, 73–88.
- Sammartino, S., A. Bouchet, D. Prêt, J.-C. Parneix, and E. Tevissen (2003), Spatial distribution of porosity and minerals in clay rocks from the Callovo-Oxfordian formation (Meuse-Haute-Marne, Eastern France)—Implications on ionic species diffusion and rock sorption capability, *Appl. Clay Sci.*, *23*, 157–166.
- Sen, P. N. (1997), Resistivity of partially saturated carbonate rocks with microporosity, *Geophysics*, *62*, 415–425.
- Sen, P. N., C. Scala, and M. H. Cohen (1981), A self-similar model for sedimentary rocks with application to the dielectric constant of fused glass beads, *Geophysics*, *46*(5), 781–795.
- Sen, P. N., W. E. Kenyon, H. Takezaki, and M. J. Petricola (1997), Formation factor of carbonate rocks with microporosity: Model calculation, *J. Pet. Sci. Eng.*, *17*(364), 345–352.
- Sihvola, A. (1996), Homogenization of a dielectric mixture with anisotropic spheres in anisotropic background, *Tech. Rep. LUTEDX/ (TEAT-7050)/1-15/(1996)*.
- Sihvola, A. (1999), *Electromagnetic Mixing Formulas and Applications*, Electromagnetic Waves Series, vol. 47, The Institution of Electrical Engineers, London, U. K.
- Sihvola, A. (2005), Metamaterials and depolarization factors, *Prog. Electromagn. Res.*, *51*, 65–82.
- Stineman, R. W. A. (1980), Consistently well-behaved method of interpolation, *Creat. Comput.*, *6*, 54–57.
- Tabbagh, A., and P. Cosenza (2007), Effect of microstructure on the electrical conductivity of clay-rich systems, *Phys. Chem. Earth, Parts A/B/C*, *32*, 154–160, doi:10.1016/j.pce.2006.02.045.
- Tabbagh, A., C. Panissod, R. Guérin, and P. Cosenza (2002), Numerical modeling of the role of water and clay content in soils' and rocks' bulk electrical conductivity, *J. Geophys. Res.*, *107*(B11), 2318, doi:10.1029/2000JB000025.
- Torquato, S., and G. Stell (1982), Microstructure of two-phase random media. I. The n -point probability functions, *J. Chem. Phys.*, *77*, 2071, doi:10.1063/1.444011.
- Van Loon, L. R., J. M. Soler, A. Jakob, and M. H. Bradbury (2003), Effect of confining pressure on the diffusion of HTO, $^{36}\text{Cl}^-$ and $^{125}\text{I}^-$ in a layered argillaceous rock (Opalinus clay): Diffusion perpendicular to the fabric, *Appl. Geochem.*, *18*, 1653–1662, doi:10.1016/S0883-2927(03)00047-7.
- Van Loon, L. R., J. M. Soler, W. Müller, and M. H. Bradbury (2004), Anisotropic diffusion in layered argillaceous rocks: A case study with Opalinus Clay, *Environ. Sci. Technol.*, *38*, 5721–5728.
- Vasin, R. N., H. R. Wenk, W. Kanitpanyacharoen, S. Matthies, and R. Wirth (2013), Elastic anisotropy modeling of Kimmeridge shale, *J. Geophys. Res. Solid Earth*, *118*, 3931–3956, doi:10.1002/jgrb.50259.
- Weber, L., J. Dorn, and A. Mortensen (2003), On the electrical conductivity of metal matrix composites containing high volume fractions of non-conducting inclusions, *Acta Mater.*, *51*, 3199–3211.
- Weiler, R. A., and J. Chaudisson (1968), Surface conductivity and dielectrical properties of montmorillonite gels, *Clays Clay Miner.*, *16*, 147–155.
- Wenk, H.-R., I. Voltolini, H. Franz, K. Nihei, and S. Nakagawa (2007), Preferred orientation and elastic anisotropy of illite-rich shale, *Geophysics*, *72*(2), E69–E75.
- Wenk, H.-R., I. Voltolini, M. Mazurek, R. Van Loon, and A. Vinsot (2008), Preferred orientations and anisotropy in shales: Callovo-Oxfordian shale (France), Opalinus Clay (Switzerland), *Clays Clay Miner.*, *56*(3), 285–306.

- Widjajakusuma, J., C. Manwart, B. Biswal, and R. Hilfer (1999), Exact and approximate calculations for the conductivity of sandstones, *Phys. A*, 270, 325–331.
- Widjajakusuma, J., B. Biswal, and R. Hilfer (2003), Quantitative comparison of mean field mixing laws for conductivity and dielectric constants of porous media, *Phys. A*, 318, 319–333.
- Woodruff, W. F., A. Revil, and C. Torres-Verdín (2014), Laboratory determination of the complex conductivity tensor of unconventional anisotropic shales, *Geophysics*, 79(5), E183–E200.
- Zisser, N., and G. Nover (2009), Anisotropy of permeability and complex resistivity of tight sandstones subjected to hydrostatic pressure, *J. Appl. Geophys.*, 68(3), 356–370.